Layered ^{4}He and ^{3}He-^{4}He mixture between two surfaces

V. Apaja[1,2] and E. Krotscheck[1]
[1]*Institut für Theoretische Physik, Johannes Kepler Universität, A-4040 Linz, Austria*
[2]*Department of Physical Sciences, Theoretical Physics, University of Oulu, FIN-90014 Oulu, Finland*
(Received 2 April 2001; published 29 August 2001)

We examine the static, dynamic, and low-temperature thermodynamic properties of liquid ^{4}He and the low-concentration limit of ^{3}He-^{4}He mixtures confined between two walls. A generalized variational Jastrow-Feenberg ansatz with time-dependent correlations is used for describing the excited states; the present variant accounts for up to three-phonon effects. We show that with decreasing wall separation the quantum liquid goes though a sequence of confined layering transitions familiar from classical fluids. These transitions are due to the geometry and have potentially observable effects in the roton excitations near wave vector $k \sim 2$ Å^{-1}. In high-density liquid ^{4}He, ^{3}He impurities assemble in the middle of the gap forming a nearly perfect two-dimensional Fermi-liquid layer.

DOI: 10.1103/PhysRevB.64.134503 PACS number(s): 67.60.Hr, 67.40.Db, 67.40.Kh

I. INTRODUCTION

We investigate in this work the physics of liquid ^{4}He confined between two walls, as well as that of ^{3}He-^{4}He mixtures in the low-concentration limit. Our model is characterized by the interaction of the ^{4}He atoms with the walls, the width of the gap between walls, and the amount of adsorbed helium. The effect of possible high-density solid layers attached to the walls is included by an effective potential; thus we concentrate on the translationally invariant *liquid.*

Squeezed liquids, although conceptually simple, exhibit a rich variety of phase transitions, such as capillary condensation[1] and layering transitions in confinement.[2] Injection of ^{3}He or ^{4}He into aerogel or Vycor glass provides an opportunity to study helium films adsorbed in a randomly interconnected porous material. Aerogels provide a means to introduce disorder into ^{3}He, leading to modification of the phase diagram of the superfluid phases. Hallock and co-workers[3–5] have demonstrated hysteresis, return-point memory, and avalanche effects in connection with capillary condensation in Nuclepore, yet another porous material.

The question of how confinement alters the elementary excitations in a liquid has been studied by inelastic neutron scattering. Recent measurements indicate that, apart from possible layer modes and a very different temperature dependence, the elementary excitation spectrum of ^{4}He in aerogel[6–8] and Vycor glass[9] is similar to that of bulk helium. Earlier estimates of the lifetime of a confined roton ranged from about 5 μeV (Refs. 7 and 10) up to 10 μeV (Ref. 11); a recent high-resolution experiment gives an upper limit of only 0.1 μeV.[12]

The confined liquid is distinguished from helium films physisorbed to a one-sided substrate[13] by an important aspect: If the number of ^{4}He particles adsorbed to a one-sided substrate is increased, helium atoms are promoted to consecutively higher layers and the film becomes thicker. The lowest-lying excitations in this geometry are surface waves. Such a layer promotion is suppressed in finite-width gaps, and the lowest-lying excitations are normally two-dimensional phonons. This provides the possibility of generating and studying a practically two-dimensional high-density quantum liquid.

Besides studies on confined quantum fluids, a wealth of information has been gathered about classical fluids between two surfaces. If one moves the surfaces closer together (or increases the number of trapped atoms), the number of liquid layers can change abruptly, i.e., layers are ''squeezed out.'' The first direct observation of such layering transitions in quasi two dimensions was recently made by Mugele and Salmeron[14] in 1-undecanol between mica surfaces, and a theoretical model has been proposed by Persson and Tosatti.[15,16] Layering transitions are of great practical interest in, for example, confined lubricants.[17] The layer structure itself gives rise to oscillatory solvation forces (forces exerted on the walls) as a function of the gap width.[18] In capillary condensation these forces change discontinuously and show hysteresis[19,20] as a function of the gap width.

To observe the layering transition in a confined liquid helium, one needs a quasi-two-dimensional environment to ensure that the number of liquid layers is sufficiently low so that the layer structure is sharp enough to have observable effects. A traditional two-wall quantum liquid confinement consists of helium injected in the space between *two silicon wafers*. Lipa *et al.*[21] and Gasparini and co-workers[22–25] have measured the ^{4}He specific heat near the λ transition. The wall separations used in Ref. 24 ranged from about 500 Å to 7000 Å (one separation for each experimental cell). The thickness of one ^{4}He layer is about 3 Å; hence one can have over 160 layers of solid or liquid ^{4}He in a gap of 500 Å. Much smaller wall separations are therefore needed in order to have a pronounced layer structure and potentially observable effects arising from such local structures.

Liquid ^{4}He squeezed between two walls can also be considered as a model of liquid helium in aerogel. Aerogel has a typical porosity between 85% and 99.5% and consists of silica strands of the order of 100 Å apart; the interconnected pores making up the strands have sizes from a few to a few hundred Å. The material is quite random, which makes clean predictions difficult. A material which might prove suitable for layering studies in a more controlled environment is *hectorite,* which consists of regular quasi-two-dimensional

smectite layers of about 9.6 Å thickness, kept some 17–20 Å apart by randomly distributed pillars made of inorganic compounds. Wada and collaborators[26–29] were the first to examine liquid ^{3}He and ^{4}He in hectorite. They have measured, among other properties, the specific heat of phonons and rotons in *partially filled* hectorite gaps.[27]

We concentrate in this work mostly on filled-gap systems, which show a very rich behavior. A direct comparison with the experiments of Wada and co-workers is difficult, because these apply, as we shall see, mostly to mixed phases containing a partly capillary condensed liquid. Although neutron scattering data are not yet available, we hope that our investigations will encourage experimental studies on this interesting system. A preliminary account of this work, together with calculations of the roton energy and the static response function, was given in Ref. 2. One potentially observable effect of confinement is a ''dip'' in the roton energy at the location of the layering transition; the reader is directed to that paper for details. Capillary condensation has been discussed[30,31] within a nonlocal density-functional theory.

Our paper is organized as follows: In Sec. II we give a brief account of the ground-state theory of inhomogeneous quantum liquids and impurity atoms solvated therein. Dynamics is discussed in Sec. III, and the extension of our theory to finite temperatures is described in Sec. IV. These parts are meant as reminders to the reader of the basic ideas and to define the notation. Complete surveys of the ground-state theory may be found in Ref. 32 or Ref. 33; excited states have been thoroughly covered in Refs. 34 and 35. In Sec. V we present results for various wall separations and look at the details for a helium liquid of 14 Å width, inspired by the hectorite environment.

II. INHOMOGENEOUS GROUND STATE

A. Pure ^{4}He

The method of choice for studying the strongly interacting quantum liquid ^{4}He is the Jastrow-Feenberg theory. We present here an outline of the theory which is published in full length in Ref. 32. It is based on the microscopic, empirical Hamiltonian

$$H=\sum_i \left[-\frac{\hbar^2}{2m}\nabla_i^2 + U_{\rm sub}(\mathbf{r}_i)\right] + \sum_{i<j} V(|\mathbf{r}_i-\mathbf{r}_j|), \quad (2.1)$$

where $V(|\mathbf{r}_i-\mathbf{r}_j|)$ is the He-He interaction. The theory will be applied only to the liquid state and therefore the ''substrate'' potential $U_{\rm sub}(\mathbf{r})$ is the net interaction due to the actual substrate *plus* the layers of solid helium on top, if any.

The ground-state wave function is written in *Jastrow-Feenberg* form

$$\Psi_0(\mathbf{r}_1,\ldots,\mathbf{r}_N)=\exp\frac{1}{2}\left[\sum_i u_1(\mathbf{r}_i)+\sum_{i<j} u_2(\mathbf{r}_i,\mathbf{r}_j) + \sum_{i<j<k} u_3(\mathbf{r}_i,\mathbf{r}_j,\mathbf{r}_k)+\cdots\right], \quad (2.2)$$

where the n-body *correlation functions* $u_n(\mathbf{r}_1,\ldots,\mathbf{r}_n)$ are determined by functional minimization of the energy:[36]

$$\frac{\delta E_0}{\delta u_n(\mathbf{r},\ldots,\mathbf{r_n})}=0. \quad (2.3)$$

The optimized hypernetted-chain Euler-Lagrange (HNC-EL) theory for inhomogeneous quantum liquids is *formally* similar to the one for the homogeneous ground state.[37–40] An attractive feature of the HNC-EL optimization is that the process does not give a result if the assumptions on the geometry of the system are inconsistent with its true physical condition. In particular, the optimization fails if some parts of the system are not in a *stable or metastable* liquid state.

In its most basic form the energy functional one is aiming to minimize contains not only the correlation functions u_n, but also the full sequence of n-body densities $\rho_n(\mathbf{r}_1,\ldots,\mathbf{r}_n)$. One usually defines dimensionless n-body distribution functions g_n via $\rho_n(\mathbf{r}_1,\ldots,\mathbf{r}_n)=\rho_1(\mathbf{r}_1)\cdots\rho_1(\mathbf{r}_n)g_n(\mathbf{r}_1,\ldots,\mathbf{r}_n)$. This serves to isolate the contributions of the one-body densities ρ_1 (the ordinary densities). Since the u_n's determine the wave function, they also determine ρ_n's and g_n's, so one needs to establish relations between these two representations, at least for $n=1$, 2, and 3. Unlike the distribution functions, the correlation functions are not observables. It is therefore desirable to eliminate these quantities and formulate the theory entirely in terms of physically observable quantities. The process of eliminating the u_n's is described in Ref. 41; it is based on the Born-Green-Yvon (BGY) equation[42] (first equation in a hierarchy of exact equations)

$$\nabla_1\rho_1(\mathbf{r}_1) = \rho_1(\mathbf{r}_1)\nabla_1 u_1(\mathbf{r}_1)+\int d^3r_2\rho_2(\mathbf{r}_1,\mathbf{r}_2)\nabla_1 u_2(\mathbf{r}_1,\mathbf{r}_2) + \frac{1}{2}\int d^3r_2 d^3r_3\rho_3(\mathbf{r}_1,\mathbf{r}_2,\mathbf{r}_3)\nabla_1 u_3(\mathbf{r}_1,\mathbf{r}_2,\mathbf{r}_3)+\cdots \quad (2.4)$$

and on the HNC equations for inhomogeneous systems,[32]

$$g_2(\mathbf{r}_1,\mathbf{r}_2)=\exp[u_2(\mathbf{r}_1,\mathbf{r}_2)+N(\mathbf{r}_1,\mathbf{r}_2)+E(\mathbf{r}_1,\mathbf{r}_2)],$$
$$h(\mathbf{r}_1,\mathbf{r}_2)=g_2(\mathbf{r}_1,\mathbf{r}_2)-1,$$
$$\tilde{N}(\mathbf{r}_1,\mathbf{r}_2)=[\tilde{h}*\tilde{X}](\mathbf{r}_1,\mathbf{r}_2),$$
$$X(\mathbf{r}_1,\mathbf{r}_2)=h(\mathbf{r}_1,\mathbf{r}_2)-N(\mathbf{r}_1,\mathbf{r}_2). \quad (2.5)$$

We have above introduced the ''tilde'' notation for any function $A(\mathbf{r},\mathbf{r}')$,

$$\tilde{A}(\mathbf{r},\mathbf{r}')\equiv\sqrt{\rho_1(\mathbf{r})}A(\mathbf{r},\mathbf{r}')\sqrt{\rho_1(\mathbf{r}')}, \quad (2.6)$$

and the asterisk denotes the convolution product:

$$[\tilde{A}*\tilde{B}](\mathbf{r}_1,\mathbf{r}_2)\equiv\int d^3r_3\tilde{A}(\mathbf{r}_1,\mathbf{r}_3)\tilde{B}(\mathbf{r}_3,\mathbf{r}_2). \quad (2.7)$$

$E(\mathbf{r}_1,\mathbf{r}_2)$ is the sum of the so-called elementary diagrams. With the BGY and HNC equations one can eliminate $u_1(\mathbf{r})$ and $u_2(\mathbf{r},\mathbf{r}')$, respectively.

The optimal triplet correlations can be expressed in terms of the one-body density $\rho_1(\mathbf{r}_1)$ and the two-body distribution function $g_2(\mathbf{r}_1,\mathbf{r}_2)$ and finally the ground-state energy can be written in the form[43]

$$E_0 = E_0[\rho_1, g_2] = T + V_{\text{ext}} + E_c . \tag{2.8}$$

Here, T is the kinetic energy of a noninteracting model system whose ground-state wave function is $\sqrt{\rho_1(\mathbf{r}_1)}$:

$$T = \frac{\hbar^2}{2m}\int d^3r |\nabla \sqrt{\rho_1(\mathbf{r})}|^2 . \tag{2.9}$$

V_{ext} is the energy of the particles in the external potential:

$$V_{\text{ext}} = \int d^3r U_{\text{ext}}(\mathbf{r})\rho_1(\mathbf{r}). \tag{2.10}$$

The ''correlation'' energy E_c can again be written as the functional of $\rho_1(\mathbf{r})$ and $g_2(\mathbf{r},\mathbf{r}')$ (see the Appendix in Ref. 43).

The variation of the energy with respect to the one-body density is done keeping the particle number N fixed:

$$\frac{\delta(E_0 - \mu N)}{\delta\rho_1(\mathbf{r})} = 0. \tag{2.11}$$

The optimization condition takes the form of a Hartree equation for $\rho_1(\mathbf{r})$,

$$\left[-\frac{\hbar^2}{2m}\nabla^2 + U_{\text{ext}}(\mathbf{r}) + V_{\text{H}}(\mathbf{r}) \right] \sqrt{\rho_1(\mathbf{r})} = \mu \sqrt{\rho_1(\mathbf{r})}, \tag{2.12}$$

where the self–consistent one-body potential is

$$V_{\text{H}}(\mathbf{r}) = \frac{\delta E_c}{\delta\rho_1(\mathbf{r})}; \tag{2.13}$$

it has a more complicated analytic structure than the ordinary Hartree potential appearing in theories of weakly interacting systems. One may think of the HNC-EL theory as of a version of density-functional theory with a highly nonlocal correlation-energy functional, whose form is derived within the theory. Another important difference is that the HNC-EL density functional *exists only for physically realizable densities*. Hence, there is no need for retrospective stability analysis. This is a valuable asset, because inhomogeneity gives rise to many phase transitions.

The two-body equation reads

$$\frac{\delta E_0}{\delta g_2(\mathbf{r},\mathbf{r}')} = \frac{\delta E_c}{\delta g_2(\mathbf{r},\mathbf{r}')} = 0. \tag{2.14}$$

Determining the pair correlations by optimization, as opposed to an ''intelligent guess'' for the pair correlation function $u_2(\mathbf{r},\mathbf{r}')$, has a number of significant advantages: First, the optimized theory is formulated entirely in terms of physical observables, e.g., the one- and two-body densities. In fact, the Euler equation can be derived, from an approximate summation of Feynman diagrams, without ever introducing the correlation functions.[44–46] Second, the optimization eliminates any prejudice on the structure of the system we might have. Third, the additional computational effort due to the optimization is insignificant relative to solving the HNC equations for a fixed trial function $u_2(\mathbf{r},\mathbf{r}')$. To summarize, there is no point in not optimizing $g_2(\mathbf{r},\mathbf{r}')$.

The two-body Euler equation is best formulated in terms of the (real-space) static structure function

$$S(\mathbf{r},\mathbf{r}') = \delta(\mathbf{r}-\mathbf{r}') + \tilde{h}(\mathbf{r},\mathbf{r}'), \tag{2.15}$$

a one-body Hamiltonian

$$H_1(\mathbf{r}) = -\frac{\hbar^2}{2m}\frac{1}{\sqrt{\rho_1(\mathbf{r})}}\nabla\rho_1(\mathbf{r})\nabla\frac{1}{\sqrt{\rho_1(\mathbf{r})}}, \tag{2.16}$$

and the so-called *particle-hole interaction* $V_{\text{p-h}}(\mathbf{r},\mathbf{r}')$. The explicit form of this effective potential follows from the HNC-EL equation; it will be given below. In an *exact* theory, i.e., when *all* diagrams are summed, and *all* n-body correlations are optimized, $V_{\text{p-h}}(\mathbf{r},\mathbf{r}')$ can equivalently be defined via

$$V_{\text{p-h}}(\mathbf{r},\mathbf{r}') \equiv \frac{\delta^2 E_c}{\delta\rho_1(\mathbf{r})\,\delta\rho_1(\mathbf{r}')} \equiv \frac{\delta V_{\text{H}}(\mathbf{r})}{\delta\rho_1(\mathbf{r}')}, \tag{2.17}$$

where the latter equality follows from Eq. (2.13). The solution of the Hartree equation corresponds to a locally stable energy minimum only if the operator resulting from second-order density variation is positive definite. Hence the eigenvalues λ in the equation

$$\left[-\frac{\hbar^2}{2m}\nabla^2 + U_{\text{ext}}(\mathbf{r}) + V_{\text{H}}(\mathbf{r}) - \mu \right] \delta\sqrt{\rho_1(\mathbf{r})} + 2\int d\mathbf{r}'\, \tilde{V}_{\text{p-h}}(\mathbf{r},\mathbf{r}')\,\delta\sqrt{\rho_1(\mathbf{r}')} = \lambda\,\delta\sqrt{\rho_1(\mathbf{r})} \tag{2.18}$$

should all be positive.

The two-body Euler equation can be written in the form

$$[S^{-1} * H_1 * S^{-1}](\mathbf{r},\mathbf{r}') = \delta(\mathbf{r}-\mathbf{r}')H_1(\mathbf{r}) + 2\tilde{V}_{\text{p-h}}(\mathbf{r},\mathbf{r}'). \tag{2.19}$$

One-body quantities such as H_1 are diagonal in this representation, and the inverse of the static structure function is to be understood in the sense of the convolution product (2.7). The explicit form for the particle-hole potential can be derived within the HNC formalism; the result is[47,48]

$$V_{\text{p-h}}(\mathbf{r},\mathbf{r}') = g_2(\mathbf{r},\mathbf{r}')[V(|\mathbf{r}-\mathbf{r}'|) + \Delta V(\mathbf{r},\mathbf{r}')] + \frac{\hbar^2}{2m}[|\nabla_1\sqrt{g_2(\mathbf{r},\mathbf{r}')}|^2 + |\nabla_2\sqrt{g_2(\mathbf{r},\mathbf{r}')}|^2] + [g_2(\mathbf{r},\mathbf{r}') - 1]w_{\text{ind}}(\mathbf{r},\mathbf{r}'). \tag{2.20}$$

The $\Delta V(\mathbf{r},\mathbf{r}')$ in Eq. (2.20) is a contribution arising from the inclusion of triplet correlations and elementary diagrams,[39,32] and $w_I(\mathbf{r},\mathbf{r}')$ is the so-called ''induced interaction'':

$$\tilde{w}_{\rm ind}(\mathbf{r},\mathbf{r}') = -\tfrac{1}{2}[H_1(\mathbf{r})+H_1(\mathbf{r}')]\tilde{N}(\mathbf{r},\mathbf{r}') + \tfrac{1}{2}[\tilde{X}^* H_1^* \tilde{X}](\mathbf{r},\mathbf{r}'). \quad (2.21)$$

The function $X(\mathbf{r},\mathbf{r}')$ is known as the direct correlation function or the sum of ''non-nodal'' Born-Mayer diagrams appearing in the HNC equations (2.5).

In the geometry adopted here, all two-body quantities are functions of the distances z,z' from the substrate and the distance $r_\parallel$ of the particles parallel to the substrate. Momentum in the parallel direction is a good quantum number, and we can, in this direction, have ordinary sound with a linear dispersion relation. In the case of one-sided adsorbed films, this sound is normally the (substrate potential driven) third sound or the (surface tension driven) ripplon. In the present case, we expect mostly longitudinal density fluctuations.

In practice, the particle-hole potential given in Eq. (2.20) is not the same as the one defined Eq. (2.17). As a consequence, quantities such as the speed of sound that can be calculated using either microscopic or macroscopic quantities will slightly disagree for all approximate theories. The hydrodynamic sound velocity is given by[49–51]

$$mc_s^2 = n\frac{d\mu}{dn}. \quad (2.22)$$

It is easy to see that Eq. (2.22) does not imply a surface excitations by noticing that in a *homogeneous* system, Eq. (2.22) reduces to the hydrodynamic relationship

$$mc_s^2 = \frac{dP}{dn}, \quad (2.23)$$

which is a *volume* excitation. In strongly confined situations the lowest-lying mode may indeed be a ''two-dimensional'' phonon. The precise physical nature of a specific excitation is revealed by the transition density and current, which will be discussed in the next section.

Differentiating Eq. (2.12) one obtains[52]

$$m\overline{c_s^2} = \frac{1}{2}\frac{n}{\{\sqrt{\rho_1}|[H_1(0+)+2\tilde{V}_{\text{p-h}}(0+)]^{-1}|\sqrt{\rho_1}\}}, \quad (2.24)$$

where $H_1(0+)$ and $\tilde{V}_{\text{p-h}}(0+)$ are the operators $H_1(z,k_\parallel)$ and $\tilde{V}_{\text{p-h}}(z,z',k_\parallel)$ in the limit $k_\parallel \to 0+$. In the bulk liquid one can prove that[53]

$$m\overline{c_s^2} \geqslant mc_s^2, \quad (2.25)$$

and one may argue[54] that this relation holds also in inhomogeneous liquids.

B. Atomic impurities

We adopt the convention that coordinate $\mathbf{r}_0$ refers to the impurity particle and coordinates $\mathbf{r}_i$, with $i=1,\ldots,N$, to the background particles. The Hamiltonian of the $(N+1)$-particle system consisting of N ^{4}He atoms and one impurity is

$$H_{N+1}^I = -\frac{\hbar^2}{2m_I}\nabla_0^2 + U_{\text{sub}}^I(\mathbf{r}_0) + \sum_{i=1}^{N} V^I(|\mathbf{r}_0-\mathbf{r}_i|) + H_N. \quad (2.26)$$

The variational wave function (2.2) for an inhomogeneous N-particle Bose system with a single impurity atom is

$$\Psi_0^I(\mathbf{r}_0,\mathbf{r}_1,\ldots,\mathbf{r}_N) = \exp\frac{1}{2}\Big[u_1^I(\mathbf{r}_0) + \sum_{1\leqslant i\leqslant N} u_2^I(\mathbf{r}_0,\mathbf{r}_i) + \sum_{1\leqslant i<j\leqslant N} u_3^I(\mathbf{r}_0,\mathbf{r}_i,\mathbf{r}_j) + \cdots\Big] \times \Psi_0(\mathbf{r}_1,\ldots,\mathbf{r}_N).$$

The impurity chemical potential is $\mu^I \equiv E_0^I - E_0$, where E_0^I is the energy of the system containing one impurity and N background atoms, and E_0 is the energy (2.8) of the unperturbed background system.

The impurity chemical potential μ^I has a structure similar to that of the background energy,

$$\mu^I = T^I + V_{\text{sub}}^I + E_c[\rho_1^I,\rho_1,g_2^I,g_2], \quad (2.27)$$

where

$$T^I = \frac{\hbar^2}{2m_I}\int d^3r_0 |\nabla\sqrt{\rho_1^I(\mathbf{r}_0)}|^2, \quad (2.28)$$

$$V_{\text{sub}}^I = \int d^3r_0 U_{\text{sub}}^I(\mathbf{r}_0)\rho_1^I(\mathbf{r}_0) \quad (2.29)$$

depend only on the impurity density $\rho_1^I(\mathbf{r}_0)$, and the correlation energy part is $E_c[\rho_1^I,\rho_1,g_2^I,g_2]$.

The usual definitions[55] of the impurity densities and distribution functions are used to derive the explicit expression for the impurity correlation energy. One must take into account that all background quantities are changed by the presence of the impurity by terms of the order of $1/N$; these changes give rise to quantitatively important rearrangement effects. The details of the derivation are given in Refs. 55 and 56.

The impurity density is calculated by minimizing the chemical potential (2.27) with respect to $\sqrt{\rho_1^I(\mathbf{r}_0)}$. This leads to the usual Hartree equation

$$\left[-\frac{\hbar^2}{2m_I}\nabla_0^2\sqrt{\rho_1^I(\mathbf{r}_0)}+U_{\rm ext}^I(\mathbf{r}_0)+V_{\rm H}^I(\mathbf{r}_0)\right]\sqrt{\rho_1^I(\mathbf{r}_0)}$$
$$=\mu^I\sqrt{\rho_1^I(\mathbf{r}_0)}. \tag{2.30}$$

The operator

$$H_1^I(\mathbf{r}_0)=-\frac{\hbar^2}{2m_I}\frac{1}{\sqrt{\rho_1^I(\mathbf{r}_0)}}\nabla_0\rho_1^I(\mathbf{r}_0)\nabla_0\frac{1}{\sqrt{\rho_1^I(\mathbf{r}_0)}}$$
$$=-\frac{\hbar^2}{2m_I}\nabla_0^2+[U_{\rm sub}^I(\mathbf{r}_0)+V_{\rm H}^I(\mathbf{r}_0)]-\mu^I \tag{2.31}$$

defines through

$$H_1^I(\mathbf{r}_0)\,\eta^{(\alpha)}(\mathbf{r}_0)=\varepsilon_\alpha\eta^{(\alpha)}(\mathbf{r}_0) \tag{2.32}$$

the spectrum ε_α and the set of states $\eta^{(\alpha)}(\mathbf{r}_0)$ which may be interpreted, in an approximation to be examined below, as excitation energies of the impurity atom.

The two-body Euler equation is derived[56,55] by variation of the impurity chemical potential with respect to $\sqrt{g_2^I(\mathbf{r}_0,\mathbf{r}_1)}$. It can be formulated in terms of the *direct correlation function* for the impurity $\tilde{X}^I(\mathbf{r}_0,\mathbf{r}_1)$, which is related to the impurity pair-distribution function through the Ornstein-Zernike relation

$$\tilde{h}^I(\mathbf{r}_0,\mathbf{r})\equiv S^I(\mathbf{r}_0,\mathbf{r})=[\tilde{X}^I*S](\mathbf{r}_0,\mathbf{r}) \tag{2.33}$$

where

$$h^I(\mathbf{r}_0,\mathbf{r})=g_2^I(\mathbf{r}_0,\mathbf{r})-1, \tag{2.34}$$

$$[H_1^I(\mathbf{r}_0)+H_1(\mathbf{r}_1)]\tilde{X}^I(\mathbf{r}_0,\mathbf{r}_1)-[\tilde{X}^I*H_1\tilde{X}](\mathbf{r}_0,\mathbf{r}_1)$$
$$=-2\tilde{V}_{\text{p-h}}^I(\mathbf{r}_0,\mathbf{r}_1). \tag{2.35}$$

The effective interaction $V_{\text{p-h}}^I(\mathbf{r}_0,\mathbf{r})$ and the induced interaction $w_{\rm ind}^I(\mathbf{r}_0,\mathbf{r})$ are structurally similar to the background expressions (2.20) and (2.21):

$$V_{\text{p-h}}^I(\mathbf{r}_0,\mathbf{r})=g_2^I(\mathbf{r}_0,\mathbf{r})[V(|\mathbf{r}_0-\mathbf{r}|)+\Delta V^I(\mathbf{r}_0,\mathbf{r})]$$
$$+\frac{\hbar^2}{2m_I}|\nabla_{\mathbf{r}_0}\sqrt{g_2^I(\mathbf{r}_0,\mathbf{r})}|^2+\frac{\hbar^2}{2m}|\nabla_{\mathbf{r}}\sqrt{g_2^I(\mathbf{r}_0,\mathbf{r})}|^2$$
$$+h^I(\mathbf{r}_0,\mathbf{r})w_{\rm ind}^I(\mathbf{r}_0,\mathbf{r}) \tag{2.36}$$

and

$$\tilde{w}_{\rm ind}^I(\mathbf{r}_0,\mathbf{r})=-\tfrac{1}{2}[H_1^I(\mathbf{r}_0)+H_1(\mathbf{r})]\tilde{N}^I(\mathbf{r}_0,\mathbf{r})$$
$$-\tfrac{1}{2}[\tilde{X}^I*H_1\tilde{X}](\mathbf{r}_0,\mathbf{r}). \tag{2.37}$$

III. DYNAMICS

In this section we will briefly review the key features of the theory for excited states of inhomogeneous quantum liquids. The dynamics of boson quantum films was described in much detail in Refs. 35 and 34; the formalism applies to the present case of ^{4}He between two walls without modifications. The goal is to find an expression for the density-density response function $\chi(\mathbf{k},\omega)$ and further the dynamic structure function

$$S(\mathbf{k},\omega)=-\frac{1}{\pi}\text{Im}\,\chi(\mathbf{k},\omega)$$
$$=-\frac{1}{\pi}\int d^3r\,d^3r'\,e^{i\mathbf{k}\cdot(\mathbf{r}-\mathbf{r}')}\text{Im}\,\chi(\mathbf{r},\mathbf{r}';\omega). \tag{3.1}$$

Our theory of the dynamic structure function is the generalization of that of Jackson[57] and Campbell[58] to inhomogeneous systems. We consider an infinitesimal, time-dependent perturbation, which drives the liquid out of its ground state:

$$\delta H(\mathbf{r}_1,\ldots,\mathbf{r}_N;t)=\sum_{i=1}^N\delta U_{\rm ext}(\mathbf{r}_i;t). \tag{3.2}$$

As a consequence, the wave function acquires time dependence. A logical extension of the Jastrow-Feenberg variational wave function to excited states is

$$|\Psi(t)\rangle=\frac{e^{-iE_0t/\hbar}e^{\delta U(t)/2}|\Psi_0\rangle}{[\langle\Psi_0|e^{\delta U(t)}|\Psi_0\rangle]^{1/2}}, \tag{3.3}$$

where $|\Psi_0\rangle$ is the ground-state wave function, E_0 is its energy, and

$$\delta U(t)=\sum_i\delta u_1(\mathbf{r}_i;t)+\sum_{i<j}\delta u_2(\mathbf{r}_i,\mathbf{r}_j;t)+\cdots \tag{3.4}$$

is the complex *excitation operator*. The time-dependent correlation functions $\delta u_n(\mathbf{r}_1,\ldots,\mathbf{r}_n;t)$ are determined by an action principle:[59,60]

$$\delta\mathcal{S}=\delta\int dt\langle\Psi(t)|H+\delta H(t)-i\hbar\frac{\partial}{\partial t}|\Psi(t)\rangle=0, \tag{3.5}$$

where the variations are taken[34,61–63] treating the $\delta u_n(\mathbf{r}_1,\ldots,\mathbf{r}_n;t)$ as independent functions.

We assume that the external perturbation is sufficiently small to permit the linearization of the equations of motion in terms of the $\delta u_n(\mathbf{r}_1,\ldots,\mathbf{r}_n;t)$. Then, dynamics can be treated within linear response theory. By keeping terms of leading order in the dynamical correlations, the resulting Euler equations can be cast in the form of coupled *equations of motion* (EOM). The conjugate variable to the time is the excitation energy $\hbar\omega$. In general it is complex; the real part gives the dispersion and the imaginary part the inverse lifetime of the excitation.

Applying the action principle to the wave function (3.3) yields the first two of the coupled equations of motion (see the Appendix of Ref. 35):

$$\frac{\hbar^2}{2m}\nabla_1\cdot\left\{\rho_1(\mathbf{r}_1)\nabla_1\delta u_1(\mathbf{r}_1;t)+\int d^3r_2\rho_2(\mathbf{r}_1,\mathbf{r}_2)\nabla_1\delta u_2(\mathbf{r}_1,\mathbf{r}_2;t)+\cdots\right\}$$

$$=-i\hbar\dot{\rho}_1(\mathbf{r}_1;t)+2\left\{\rho_1(\mathbf{r}_1)U_{ext}(\mathbf{r}_1;t)+\int d^3r_2[\rho_2(\mathbf{r}_1,\mathbf{r}_2)-\rho_1(\mathbf{r}_1)\rho_1(\mathbf{r}_2)]U_{ext}(\mathbf{r}_2;t)\right\} \tag{3.6}$$

and

$$\frac{\hbar^2}{2m}\nabla_1\cdot\left\{\rho_2(\mathbf{r}_1,\mathbf{r}_2)\nabla_1[\delta u_1(\mathbf{r}_1;t)+\delta u_2(\mathbf{r}_2,\mathbf{r}_2;t)]+\int d^3r_3\rho_3(\mathbf{r}_1,\mathbf{r}_2,\mathbf{r}_3)\nabla_1\delta u_2(\mathbf{r}_1,\mathbf{r}_3;t)+\cdots\right\}+\text{same for}\quad(1\leftrightarrow2)$$

$$=-i\hbar\dot{\rho}_2(\mathbf{r}_1,\mathbf{r}_2;t)+2\rho_2(\mathbf{r}_1,\mathbf{r}_2)[U_{ext}(\mathbf{r}_3;t)+U_{ext}(\mathbf{r}_3;t)]+2\int d^3r_3[\rho_3(\mathbf{r}_1,\mathbf{r}_2,\mathbf{r}_3)-\rho_2(\mathbf{r}_1,\mathbf{r}_2)\rho_1(\mathbf{r}_3)]U_{ext}(\mathbf{r}_3;t). \tag{3.7}$$

In the above equations the ellipsis indicates terms with fluctuations in u_3, u_4, etc. The EOM have the form of coupled continuity equations: The quantities in curly brackets on the left-hand sides are the *transition currents* and the time derivatives are those of the corresponding *transition densities*. They play a central role in identifying excitations because they contain direct information of where in the liquid a specific excitation is taking place and how particles move.

The steps leading from the exact EOM (3.6) and (3.7) to a set of technically manageable equations have been outlined in the Appendix of Ref. 35. There is no need for repetition; we only sketch briefly what remains to be done. So far the EOM are in a mixed form, and the left-hand sides contain δu_n while the time derivatives of the n-body densities are most naturally written in terms of $\delta\rho_n$. Restricting ourselves to one- and two-body quantities, one can make use of the functional expansions

$$\delta\rho_1(\mathbf{r}_1;t)=\int d^3r_2\left[\frac{\delta\rho_1(\mathbf{r}_1)}{\delta u_1(\mathbf{r}_2)}\right]\delta u_1(\mathbf{r}_2;t)+\int d^3r_2d^3r_3\left[\frac{\delta\rho_1(\mathbf{r}_1)}{\delta u_2(\mathbf{r}_2,\mathbf{r}_3)}\right]\delta u_2(\mathbf{r}_2,\mathbf{r}_3;t) \tag{3.8}$$

and

$$\delta g_2(\mathbf{r}_1,\mathbf{r}_2;t)=\int d^3r_3\frac{\delta g_2(\mathbf{r}_1,\mathbf{r}_2)}{\delta\rho_1(\mathbf{r}_3)}\delta\rho_1(\mathbf{r}_3;t)+\int d^3r_3d^3r_4\frac{\delta g_2(\mathbf{r}_1,\mathbf{r}_2)}{\delta u_2(\mathbf{r}_3,\mathbf{r}_4)}\delta u_2(\mathbf{r}_3,\mathbf{r}_4;t). \tag{3.9}$$

The functional derivatives can be evaluated using the definition of the one-body density for a known wave function and the HNC equations. As a final result, the EOM in the approximation used in the present work have $\{\delta\rho_1(\mathbf{r}_1;t),\delta u_2(\mathbf{r}_1,\mathbf{r}_2;t)\}$ as independent variables.

A. Feynman approximation

The truncation of the excitation operator in Eq. (3.4) defines the level of approximation in which we treat the excitations. The simplest approximation, which ignores all fluctuating correlation functions except $\delta u_1(\mathbf{r};t)$, is referred to, hereafter, as the *Feynman approximation*. In this case, the resulting ω is real. This is a reasonable approximation as long as the wavelength of the excitation is large compared to the average particle spacing; in particular, it is exact in the long-wavelength limit. Already at the most basic level of the Feynman theory the *single*-phonon–maxon–roton dispersion curve in the bulk is replaced by a *set* of modes in restricted geometries.

Assuming harmonic time dependence, $\delta u_1(\mathbf{r};t)=\delta u_1(\mathbf{r})e^{i\omega t}$, and abbreviating $\psi^{(n)}(\mathbf{r})=\sqrt{\rho_1(\mathbf{r})}\,\delta u_1^{(n)}(\mathbf{r})$ the action principle (3.5) may be represented as the generalized eigenvalue problem

$$H_1(\mathbf{r})\psi^{(n)}(\mathbf{r})=\hbar\omega_n\int d^3r'S(\mathbf{r},\mathbf{r}')\psi^{(n)}(\mathbf{r}'). \tag{3.10}$$

Using Eq. (3.8) one can show that the density fluctuation $\delta\rho_1^{(n)}(\mathbf{r})$ associated with the dispersion branch n is simply

$$\delta\rho_1^{(n)}(\mathbf{r})=\frac{1}{2}\sqrt{\rho_1(\mathbf{r})}\,\phi^n(\mathbf{r})=\frac{1}{2\hbar\omega_n}\sqrt{\rho_1(\mathbf{r})}H_1(\mathbf{r})\psi^{(n)}(\mathbf{r}). \tag{3.11}$$

In the bulk limit the structure factor $S(\mathbf{r},\mathbf{r}')$ can be Fourier transformed to $S(k)$ and one recovers the well-known Feynman dispersion relation $\hbar\omega(k)=\hbar^2k^2/[2mS(k)]$; all modes ω_n collapse in this case to one single mode.

The Feynman approximation corresponds here to the random phase approximation (RPA), and from the density fluctuations we construct the density-density response function

$$\chi^{\mathrm{RPA}}(\mathbf{r},\mathbf{r}',\omega)=\sum_{s,t}\delta\rho_1^{(s)}(\mathbf{r})[G_{st}^{\mathrm{RPA}}(\omega)+G_{st}^{\mathrm{RPA}}(-\omega)]\delta\rho_1^{(t)}(\mathbf{r}'), \tag{3.12}$$

where

$$G_{st}^{\mathrm{RPA}}(\omega)=\frac{\delta_{st}}{\hbar(\omega-\omega_s+i\epsilon)} \tag{3.13}$$

is the Green's function for a free Feynman phonon. Just like its bulk counterpart, the Feynman excitations in an inhomogeneous liquid satisfy the ω^0 (or zeroth moment) sum rule; in other words, the frequency integration

$$S(\mathbf{r},\mathbf{r}')=-\frac{1}{\sqrt{\rho_1(\mathbf{r})\rho_1(\mathbf{r}')}}\int_0^\infty\frac{d(\hbar\omega)}{\pi}\mathrm{Im}\,\chi^{\mathrm{RPA}}(\mathbf{r},\mathbf{r}';\omega)$$

$$=\sum_s\frac{\delta\rho_1^{(s)}(\mathbf{r})\,\delta\rho_1^{(s)}(\mathbf{r}')}{\sqrt{\rho_1(\mathbf{r})\rho_1(\mathbf{r}')}} \tag{3.14}$$

gives exactly the ground-state static structure function. This is a necessary (although not sufficient) condition that the excited states and the ground state correspond to the same Hamiltonian. A violation of self-consistency at this level would cause all subsequent calculations to be inconsistent.

B. Correlated basis functions

Subsequent to the work of Feynman,[64] Feynman and Cohen,[65] Chang and Campbell,[66] and Jackson and Feenberg[67,68] showed that, while the original Feynman theory[64] is qualitatively correct, higher-order scattering processes (involving multiple Fourier components) are essential for a full understanding of the excitation spectrum. In the short-wavelength regime (above 1.0 Å^{-1}) the Feynman approximation overestimates the excitation energy, and keeping $\delta u_2(\mathbf{r}_i,\mathbf{r}_j;t)$ leads to a significant lowering of the excitation energy.[61–63,69]

A full solution of the equations of motion for fluctuating pair correlations is, in a restricted geometry, numerically very time consuming and approximations are necessary. The approximation that we will use is tantamount to keeping what is conventionally called ''three-phonon scattering processes.'' We use the term ''phonon'' loosely; it may, for example, stand for a layer phonon or a surface mode. While excitations in the Feynman approximation have infinite lifetime, three-phonon processes allow the decay if energy and momentum are conserved. As a part of the evaluation of $\delta u_2(\mathbf{r}_i,\mathbf{r}_j;t)$ from the second EOM, we obtain the three-phonon scattering matrix elements; i.e., the probability amplitudes for the decay of one ''phonon'' into two. The second effect—mode coupling via three-phonon processes—renormalizes the mode energies. The physical character of the various Feynman modes differs considerably; this plays an important role in determining the amount by which a particular mode is renormalized.

Three-phonon processes lead to a self-energy correction

$$\Sigma_{st}^{\mathrm{CBF}}(\omega)=\frac{1}{2}\sum_{mn}\frac{\tilde{V}_{mn}^{(s)}\tilde{V}_{mn}^{(t)}}{\hbar(\omega_m+\omega_n-\omega)}, \tag{3.15}$$

which was derived, in the bulk liquid, by Chang and Campbell using Brillouin-Wigner (BW) perturbation theory with correlated basis functions (CBF's); hence the abbreviation CBF-BW is often used for this approximation. In Eq. (3.15) the summations are over all Feynman states and the three-phonon vertices $V_{mn}^{(s)}$ are determined by the second EOM (see the Appendix of Ref. 35). In order to get the expression for the CBF density-density response function one only needs to add the self-energy correction to the Green's function in Eq. (3.13),

$$G_{st}^{\mathrm{CBF}}(\omega)=[\hbar(\omega-\omega_t+i\epsilon)\,\delta_{st}+\Sigma_{st}^{\mathrm{CBF}}(\omega)]^{-1}, \tag{3.16}$$

and use it in an equation similar to Eq. (3.12).

The self-energy correction given in Eq. (3.15) decreases with increasing ω rapidly enough not to affect the zeroth- and first-moment sum rules discussed in connection with the Feynman theory. However, this form of the self-energy reveals one deficit in the approximate solution of the EOM (3.6) and (3.7): The energy denominator does not use the self-energy-corrected spectrum, but only their Feynman approximations. It should be emphasized that this is not a problem of the EOM themselves, but rather a technicality to keep the numerical effort at a reasonable level. In bulk systems, a more complete form of the self-energy has already been applied.[69] However, it is considerably more complicated than the present self-energy and is expected to lead only to quantitative improvements, but not to qualitatively new effects. We use therefore the above simpler form and keep in mind that the high-momentum excitations have somewhat too high energies.

C. Impurity dynamics

The equations of motion for time-dependent impurity correlations are derived in exactly the same manner as in the background theory; the analysis will also clarify the interpretation of the eigenvalues $\varepsilon_{\boldsymbol{\alpha}}$ of Eq. (2.32). We write

$$|\Psi^I(t)\rangle=\frac{e^{-iE_0^I t/\hbar}e^{\delta U^I(t)/2}|\Psi_0^I\rangle}{[\langle\Psi_0^I|e^{\delta U^I(t)}|\Psi_0^I\rangle]^{1/2}}, \tag{3.17}$$

where

$$\delta U^I(t)=\delta u_1(\mathbf{r}_0;t)+\sum_i\delta u_2(\mathbf{r}_0,\mathbf{r}_i;t)+\cdots. \tag{3.18}$$

The time-dependent components of the wave function are again determined by an action principle of the form (3.5) with the only qualification that the perturbing Hamiltonian $\delta H(t)$ act on the impurity atom alone. The equations of motion are also of the structure (3.6) and (3.7); they may be found in Ref. 70. Again, the level of approximation is defined by the fluctuating multiparticle correlations retained in $\delta U^I(t)$.

The simplest case is $\delta u_n(\mathbf{r}_0,\mathbf{r}_n;t)=0$ for $n\geqslant 2$. In fact, this case is trivial since it leads immediately to the interpretation of the $\eta^{(\boldsymbol{\alpha})}(\mathbf{r}_0)$ defined in Eq. (2.32) as the wave functions and the energies $\varepsilon_{\boldsymbol{\alpha}}$ as an approximation for the impurity excitation energies.

However, much physics is missing in that case: In the quasi-two-dimensional geometry, the state is characterized by the quantum number $\boldsymbol{\alpha}=\{\alpha,\mathbf{k}_\parallel\}$ where α is a discrete quantum number associated with the motion in z direction

and $\mathbf{k}_\parallel$ is the linear wave number in the x-y plane. The eigenfunctions of Eq. (2.32) have the simple form

$$\eta^{(\alpha)}(\mathbf{r}) = \eta_\alpha(z) e^{i\mathbf{k}_\parallel \cdot \mathbf{r}_\parallel} \tag{3.19}$$

and the associated energies are

$$\varepsilon_{\boldsymbol{\alpha}} = \epsilon_\alpha + \frac{\hbar^2 k_\parallel^2}{2m_I}; \tag{3.20}$$

in other words the motion of the impurity in the x-y plane is that of a free particle.

When fluctuating pair correlations are included, the equation of motion (2.32) is supplemented by a nonlocal, energy-dependent self-energy term

$$H_1^I(\mathbf{r})\psi_\omega(\mathbf{r}) + \int d^3r' \Sigma(\mathbf{r},\mathbf{r}';\omega)\psi_\omega(\mathbf{r}') = \hbar\omega\psi_\omega(\mathbf{r}). \tag{3.21}$$

The self-energy $\Sigma(\mathbf{r},\mathbf{r}';\omega)$ describes three-body processes; it has the form

$$\Sigma(\mathbf{r},\mathbf{r}',\omega) = \sum_{\alpha m} \frac{W_{m\alpha}(\mathbf{r}) W_{m\alpha}(\mathbf{r}')}{\hbar\omega - \hbar\omega_m - \epsilon_\alpha}, \tag{3.22}$$

where $W_{m\alpha}(\mathbf{r})$ is the three-body vertex function describing the coupling between an incoming ^{3}He particle to an outgoing ^{3}He in the state α as well as an outgoing phonon in state m. The detailed form of these matrix elements follows from the microscopic theory that has been described at length in Ref. 55; its detailed structure is irrelevant for the present considerations.

The additional physics introduced by the self-energy are ''backflow'' correlations at low energies, as well as potential damping of the impurity motion by coupling to phonons and rotons in the appropriate energy regime. We are here only interested in low-energy properties. In the limit $\omega \to 0^+$, the impurity motion in the parallel direction can be characterized by an effective mass, i.e., the dispersion relation resulting from solving Eq. (3.21) in our geometry and for low energies is characterized by an effective mass m_I^*:

$$\hbar\omega(k_\parallel) = \mu^I + \frac{\hbar^2 k_\parallel^2}{2m_I^*}. \tag{3.23}$$

Note the important fact that the impurity *binding energy* is not changed by the self-energy corrections. The effective mass ratio m_I^*/m_I can be expressed in closed form as[55]

$$\frac{m_I}{m_I^*} = 1 - \frac{\hbar^2}{4m_I} \sum_m \int \frac{d^2q_\parallel}{(2\pi)^2} q_\parallel^2 \frac{|X_m^I(q_\parallel)|^2}{\hbar\omega_m(q_\parallel) + \hbar^2 q_\parallel^2/2m_I}, \tag{3.24}$$

where the matrix elements $X_m^I(q_\parallel)$ are

$$X_m^I(q_\parallel) = \int dz_0 dz \sqrt{\rho_I(z_0)} \tilde{X}^I(z_0, z; q_\parallel) \phi_m(z, q_\parallel) \tag{3.25}$$

and $\phi_m(z,q_\parallel)$ is the Feynman density fluctuation associated with the dispersion branch m.

IV. THERMODYNAMICS

There are various ways to generalize the variational theory to finite temperatures. The first successful step was taken by Campbell and collaborators[71–73] who generalized the Jastrow-Feenberg variational wave function to a variational density matrix and used the Gibbs-Delbrück-Moliére principle for the Helmholtz free energy to derive practical methods for calculating the free energy, the entropy, and related thermodynamic quantities. The theory was generalized to inhomogeneous geometries in Ref. 48.

It is, again, sufficient to display only the working formulas of the theory and to point out the places where the basic equations are modified by temperature effects. The two-body equation (2.19) contains an explicit thermal term in addition to the implicit temperature dependence through $\rho_1(\mathbf{r})$ and $g_2(\mathbf{r}_1,\mathbf{r}_2)$; its finite-temperature version is

$$[S^{-1} * H_1 * S^{-1}](\mathbf{r},\mathbf{r}') = \delta(\mathbf{r}-\mathbf{r}')H_1(\mathbf{r}) + 2[\tilde{V}_{\text{p-h}}(\mathbf{r},\mathbf{r}') + \tilde{\Phi}(\mathbf{r},\mathbf{r}')], \tag{4.1}$$

where the temperature-dependent correction $\Phi(\mathbf{r},\mathbf{r}')$ is defined by

$$\tilde{\Phi}(\mathbf{r},\mathbf{r}') \equiv -2\sum_m n_m[n_m+1]\hbar\omega_m^* \psi^{(m)}(\mathbf{r})\psi^{(m)}(\mathbf{r}'), \tag{4.2}$$

with the boson occupation numbers $[\beta = (k_B T)^{-1}]$

$$n_m = \frac{1}{e^{\beta\hbar\omega_m} - 1}, \tag{4.3}$$

and the $\psi^{(m)}(\mathbf{r})$ defined in the Feynman eigenvalue problem (3.10).

The induced interaction is formally the same as displayed in Eq. (2.21); the finite-temperature particle-hole interaction $V_{\text{p-h}}(\mathbf{r},\mathbf{r}')$ is obtained from Eq. (2.20) by replacing

$$w_{\text{ind}}(\mathbf{r},\mathbf{r}') \to w_{\text{ind}}(\mathbf{r},\mathbf{r}') + \Phi(\mathbf{r},\mathbf{r}') \tag{4.4}$$

in the last term.

Details on the execution of the theory and the discussion of low-temperature limits and surface broadening may be found in Ref. 48. The entropy turns out to be that of noninteracting quasiparticles with the Feynman spectrum $\hbar\omega_m$:

$$\mathcal{S} = k_B \sum_m [(n_m+1)\ln(n_m+1) - n_m \ln n_m]. \tag{4.5}$$

In closing this section we should mention that an extension of the theory[74] allows for multiparticle correlations. When such effects are included, the Feynman excitation energies $\hbar\omega_m$ are replaced by the poles of the CBF Green's function $G_{st}^{\text{CBF}}(\omega)$ defined in Eq. (3.16). That way, a more realistic representation of the thermodynamic features above temperatures of 1 K can be obtained. The theory has, however, not been implemented in inhomogeneous geometries.

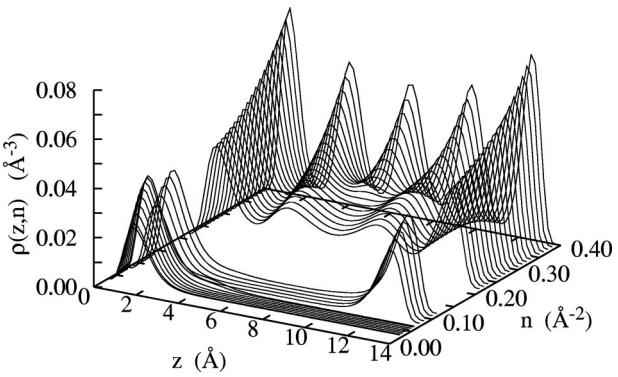

FIG. 1. Density profiles of ^{4}He in a 14-Å-wide gap are shown as function of areal density *n*. The free spaces correspond to densities where no stable liquid configurations exist.

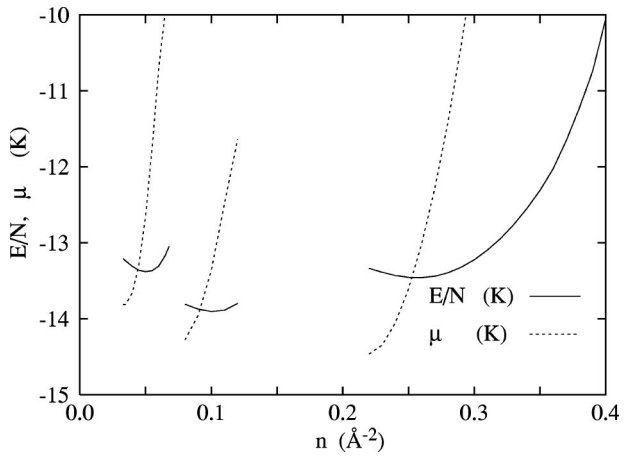

FIG. 2. The energy per particle of ^{4}He in a 14-Å-wide gap (solid lines) and the chemical potential (dashed lines) are shown as a function of areal density *n*. The distinct regions correspond, from left to right, to a monolayer, a symmetric double layer, and filling of the gap.

V. RESULTS

A. Static properties

We focus our main attention on a system with a wall separation of 14 Å because this is in reasonable agreement with the physical situation found in the gaps of hectorite. These are typically 20 Å wide; a monolayer of solid ^{4}He is attached to each side. The interaction of ^{4}He particles with the walls can be described by the usual 3-9 potential obtained from averaging Lennard-Jones potentials over a half space:

$$U_{3\text{-}9}(z)=\left[\frac{4C_3^3}{27D^2}\right]\frac{1}{z^9}-\frac{C_3}{z^3}. \tag{5.1}$$

The full external potential for a gap of width L is then

$$U_{\rm sub}(z)=U_{3\text{-}9}(z)+U_{3\text{-}9}(L-z). \tag{5.2}$$

This assumes that the walls are smooth and, hence, $U_{\rm sub}(\mathbf{r})$ is a function of one coordinate only. This does not compromise the results of our calculations because most of the lateral structure of the substrate will be smoothed out by the first solid layer of helium atoms. The potential will be suited to apply for hectorite. To determine the parameters of the 3-9 potential (5.1), we have taken long-ranged z^{-3} tail from the silicon-helium interaction,[75] $C_3=2000$ K Å^{-3}, and have adjusted the short-ranged z^{-9} repulsion such that the binding energy of single ^{4}He atoms[27] is reproduced. This gives a well depth of $D=128$ K. The substrate attraction is weaker than that of graphite, but still strong enough to cause the first atomic layer of ^{4}He to solidify. We have taken this into account by adding, as described in Ref. 32, an inert solid monolayer of ^{4}He with a thickness of 3.3 Å and surface coverage of 0.07 Å^{-2} to both walls. The picture is consistent with the fact[27] that superfluidity sets in at a filling of 1.33 layers: One layer is solid, and it takes a certain amount of ^{4}He to form a complete, low–density second layer. Since the distance between the hectorite walls is about 17–20 Å,[27] one has a liquid phase of 11–14 Å width. From now on we use the terms ''gap width'' or ''wall separation'' to designate the width of the free space available for *liquid* helium. If the actual distance between the bare substrate surfaces is meant, we will state it explicitly.

Let us first describe the scenario of filling a 14-Å gap with liquid ^{4}He. The evolution of the density profile is depicted in Fig. 1. As a function of coverage *n* one has the following filling situations.

(i) $n=0$–0.032 Å^{-2}: There is not enough helium to form a translationally invariant liquid, patches of helium can form on either wall.

(ii) $n=0.032$–0.068 Å^{-2}: One of the two walls is covered with an atomic monolayer or both walls with patches of ^{4}He. With gap width of 14 Å this configuration is probably metastable (see the energetics in Fig. 2).

(iii) $n=0.068$–0.122 Å^{-2}: Both walls are covered with atomic monolayers, but due to interaction, it is more appropriate to call it a symmetric double layer. As expected, this occurs for areal densities above at least *twice* spinodal density of a single monolayer, which is about 0.032 Å^{-2} (Refs. 76 and 77) at zero temperature. This value is also close to the areal density where a single atomic monolayer becomes unstable against the promotion of particles to a second layer.

(iv) $n=0.122$–0.22 Å^{-2}: No stable liquid phase could be found. The interaction between the two sides is strong enough such that configurations where one of the walls is covered by a double-layer would undergo capillary condensation.

(vi) $n=0.22$–0.29 Å^{-2}: The gap is completely filled with *four* liquid layers.

(vii) $n=0.29$–0.41 Å^{-2}: The gap is completely filled with *five* liquid layers.

(vii) *n* above 0.41 Å^{-2}: No stable liquid phase; presumably the layers next to the walls solidify or solid helium fills the whole gap.

One of the most remarkable features is the *confined layering transition* at the coverage $n\approx 0.29$ Å^{-2}: Near this density the film changes abruptly from four to five layers.[2]

The structure of the system is determined by the energet-

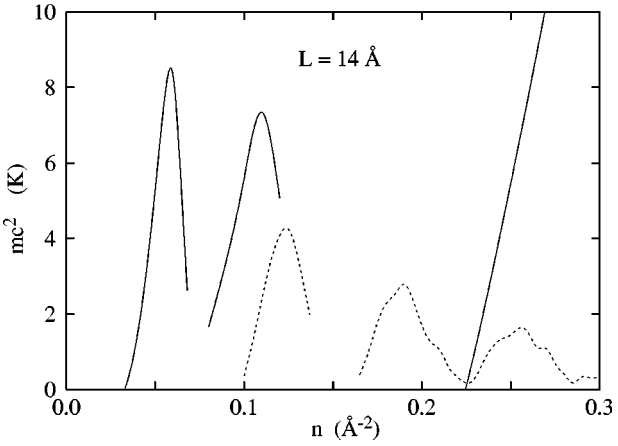

FIG. 3. The speed of longitudinal sound as a function of areal density n (solid lines). Also shown is the speed of third sound on a one-sided substrate with the same potential (dashed line). The leftmost branch corresponds to a single monolayer, for which the two sound velocities are equal.

ics, shown in Fig. 2. All three configurations discussed above—the monolayer, the symmetric double layer, and the filled gap—have their own energy minimum; the slight mismatch between the chemical potential and the energy at its minimum is due to numerics. Most notable is again the gap between $n=0.12$ Å^{-2} and $n=0.22$ Å^{-2} where no stable systems exist that are translationally invariant in the direction parallel to the walls. The configuration in this density area is to be found by means of the usual Maxwell construction.

Most directly affected by the confinement and by the interplay between stable and unstable configurations is the speed of longitudinal sound, c_s, or the longitudinal incompressibility mc_s^2. Figure 3 shows mc_s^2 as a function of coverage; we have calculated this quantity from the long-wavelength limit of the excitation spectrum (2.24) and not

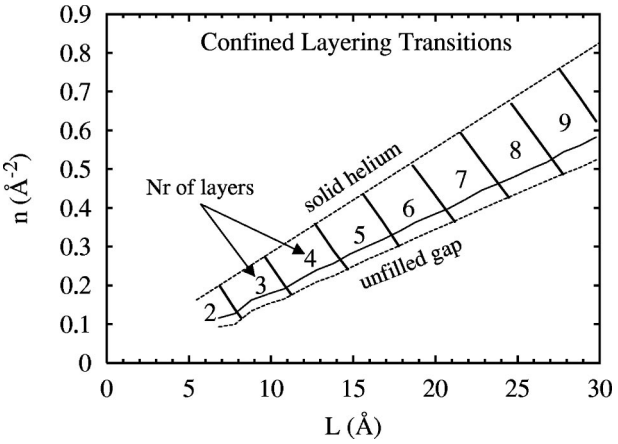

FIG. 4. The sequence of confined layering transitions in a L-n plane, i.e., gap width vs areal density. The density is limited from below by the spinodal line (lower dashed line) and from above by the freezing line (upper dashed line). The solid line crossing the transition lines is the fixed-n equilibrium; the fixed-L equilibrium lies above it (not shown).

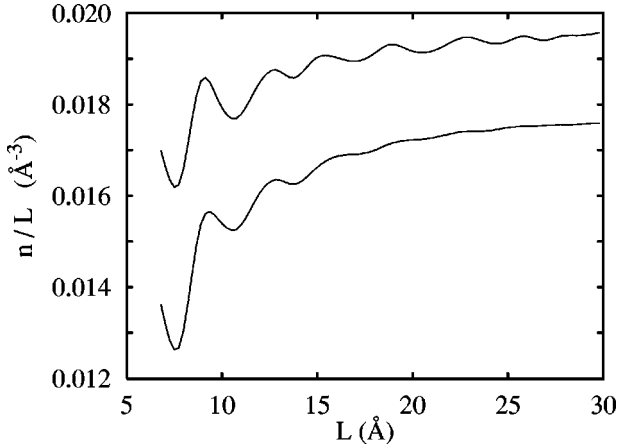

FIG. 5. The equilibrium (upper curve) and the spinodal (lower curve) areal densities divided by the gap width L. The layering transitions occur at the local minima.

from $d\mu/dn$ since the long-wavelength limit determines the regime of existence of solutions of the HNC-EL equations. The figure also shows mc_s^2 for the case where ^{4}He is adsorbed on a one-sided substrate with the same potential. The results are identical for a single monolayer filling, but start to deviate for the case of two layers: The physically interesting aspect here is not that there is a difference between the two-wall geometry and the one-sided substrate, but rather that the double-layer configuration in the hectorite is *not* identical to that of two monolayers. This is evidently a first sign of interaction between the monolayers on opposite walls. The speed of sound for configurations in the high-density regime, where the lowest excitations are longitudinal phonons, is expectedly very different from that in a multilayer adsorbed film where the lowest excitations are ripplons.

The confined layering transitions are worth examining in detail. Insight into its mechanism might be found by considering the transition as a function of the gap width. Figure 4 shows the ''phase diagram'' of the transitions between gap widths 7 and 30 Å. With a large gap in excess of 30 Å the numerical solution of the inhomogeneous HNC-EL equations becomes more and more time consuming and also the density profile is less interesting with a flat portion in the middle of the gap. According to a simulation performed recently by Heni and Lowen,[78] *crystalline* layers of hard spheres confined between two patterned substrates go through a sequence of layering transitions resembling those found for liquid helium in this work (see Fig. 3 in Ref. 78).

The transitions from two to three layers up to the transition from 9 to 10 layers obey very accurately the rule

$$n_{\mathrm{cr}}=0.252i-0.0578L+0.075, \tag{5.3}$$

where i is the number of layers in the fewer-layer phase and length is in units Å. Thus the transitions form a set of evenly spaced, parallel lines in the L-n plane (marked with straight, solid lines in Fig. 4). The layering transitions are due to the geometry and the short-range repulsion of the He-He interaction; they take place at a slightly higher areal density if the substrate potential is turned off.

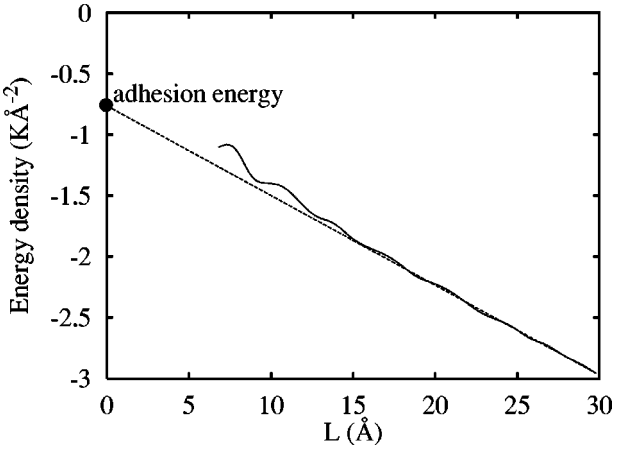

FIG. 6. Energy per unit area per wall as a function of the gap width L. From the large-L limit (straight line) we deduce the adhesion energy $E_{\mathrm{adh}} \approx 0.76$–$0.77$ K Å^{-2} of the substrate.

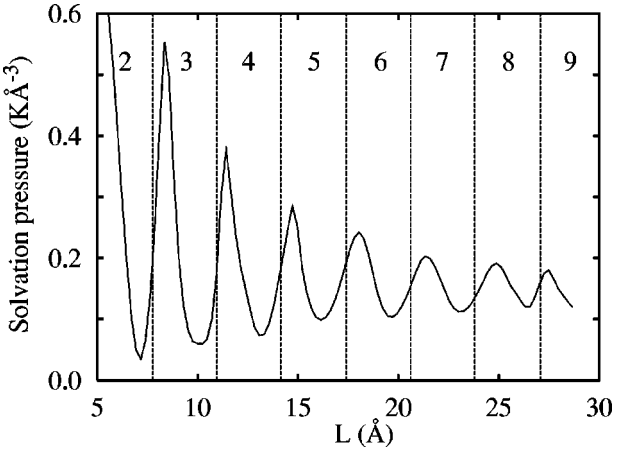

FIG. 7. The pressure exerted on the walls in the fixed-L equilibrium. The vertical lines mark the locations of the layering transitions.

The confined liquid has two equilibria corresponding to different boundary conditions: (i) minimum $E(n)$ at fixed L and (ii) minimum $E(L)$ at fixed n. The former is the equilibrium in a situation where the addition of helium does not change the gap width appreciably, which probably is the case in hectorite. The fixed areal density in the latter case can result from periodic boundary conditions or walls with very weak substrate potential in the x and y directions. Schematically, the gap could be varied in this case with a piston moving in the z direction.

Many quantities scale with the gap width L in the $L \to \infty$ limit. Figure 5 shows how the spinodal and equilibrium densities approach the scaling limit. The spinodal point is an instability in the infinite-wavelength sound mode. As the gap width increases, this mode changes from a two-dimensional to a bulk phonon. It is difficult to carry out calculations close to the spinodal instability points because all correlations become very long ranged. The present spinodal data extrapolate in the limit $L \to \infty$ to $\rho_{\mathrm{sp}} \approx 0.018$ Å^{-3}, which is slightly above the bulk value ~ 0.0168 Å^{-3}. The equilibrium density extrapolates to $\rho_{\mathrm{equil}} \approx 0.020$ Å^{-3}, which is below the known bulk value 0.021 86 Å^{-3}. The freezing density cannot be found reliably using the methods used in this paper, but the highest areal densities where a (meta)stable liquid solution is found gives an approximate upper limit to the freezing line (see Fig. 4). The energy per particle at the fixed-n equilibrium has the limiting value $E/N \approx -7.13$ K, which is close to the bulk value -7.17 K. The energy per unit area, on the other hand, gives the interfacial adhesion energy, as depicted in Fig. 6. For the present substrate plus one layer of solid helium we obtained the value $E_{\mathrm{adh}} \approx 0.76$–$0.77$ K Å^{-2}.

If the liquid is at the fixed-n equilibrium, it is off the fixed-L equilibrium. This gives rise to the so-called solvation pressure (or force), i.e., pressure exerted on the walls by the liquid, given by

$$P_n(L) = -n\left(\frac{\partial(E/N)}{\partial L}\right)_{n,N}. \tag{5.4}$$

From what is known about classical liquids one expects to see oscillations in the force as a function of the gap width, with the maxima matching the occurrence of well-formed layers.[18] Figure 7 shows that this is largely true also for helium, although the large zero-point motion of helium atoms allows them to move past each other more easily than their classical counterparts.

Although the locations of the transitions follow the same rule, they are not quite the same. With increasing L, if the number of layers changes from even to odd, a *new layer is created* between the two midmost layers. The transition from odd to even number of layers occurs via *bifurcation of an*

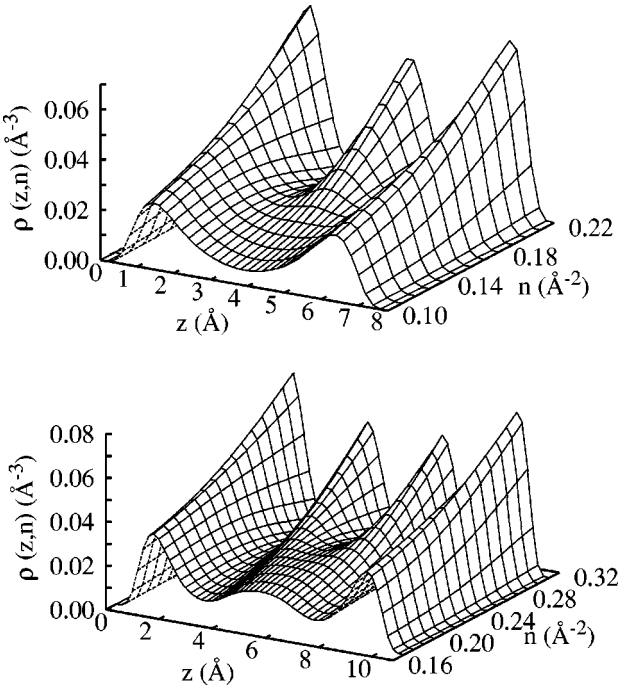

FIG. 8. Density profiles of ^{4}He in gaps of widths 8 Å (upper figure) and 11 Å (lower figure) as a function of areal density n. These are prototypes of transitions from even to odd and odd to even number of layers as n increases.

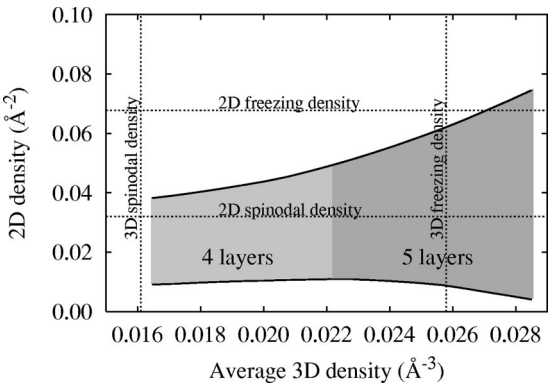

FIG. 9. The density of ^{4}He layers compared with the 2D and 3D critical densities. The gray-shaded area between the solid lines presents the range of densities found in a 14-Å-wide gap for the four- and five-layer configurations. We plot the 2D density of thin slices taken parallel to the surfaces [same as $\rho(z)$ for a fixed z] against the average 3D density (here equal to coverage/14 Å). The vertical lines are the spinodal and freezing densities of bulk 3D ^{4}He, and the horizontal lines are those of 2D ^{4}He.

existing middle layer. An example of both types is shown in Fig. 8. In some cases the closeness of the freezing density forces the transition to take place in a narrow areal density range. As a result, the fingerprints of the layering transitions in quantities such as the roton parameters are not the same for all transitions.

Some light can be shed on the stability limits of the liquid emerging from the present calculation by comparing them with the known two-dimensional (2D) and 3D critical points. In Fig. 9 the gray-shaded area covers local liquid densities found in the filled gap of 14 Å width, but the result applies to all other gap widths as well. We have left out the low-density regions between the surfaces and the first layer, and concentrate on regions where the substrate potential is less governing. The x axis of the graph in Fig. 9 represents the average 3D density, that is, the coverage divided by the gap width. The y axis plots the 2D densities $\rho(z)$ parallel to the surfaces. This quantity would describe the system if it consisted of noninteracting 2D systems stacked between the walls and one could treat each slice as an individual 2D system. At high coverages, the liquid solution was found only up to about $n=0.41$ Å^{-2}, which corresponds to the average 3D density 0.029 Å^{-3}). The highest 2D density is found in layers nearest to the walls, 0.075 Å^{-2}. We emphasize that these limits are the points where the optimal liquid structure ceases to exist, and they are always higher than the real freezing densities, the overshoot being about 20% in bulk 3D liquid and about 6% in 2D helium. Taking this into account we conclude that the high-coverage stability limit of the liquid found in the present calculation can be attributed to freezing. Technically, if one assumes that the high-coverage limit is due to freezing of the layers nearest to the walls, then one should — at least in principle — be able to go on with the liquid calculation by taking *two* solid layers of helium on both walls instead of just one.

The spinodal point is an instability against *long-wavelength* density oscillations and is therefore insensitive to local density variations; therefore we expect to see that the low-density region is limited by the 3D spinodal point at about 0.016 Å^{-3}. Indeed, this is very close to the lowest average 3D density given by left edge of the gray-shaded area in Fig. 9 at about 0.0162 Å^{-3}.

Although the *average* 3D density always stays above the bulk spinodal point in the filled-gap configuration, the *local* density between the layers goes well below it. For example, in the 14-Å gap system the lowest value is only 0.010 Å^{-3}. This might give a change to experimentally verify the critical behavior of the spinodal point of two-dimensional helium, which is not characterized by a critical exponent, but rather by the form[76]

$$\rho-\rho_s \propto c^4 \ln c \quad \text{as} \quad c \to 0+. \tag{5.5}$$

As discussed in Ref. 76, a further complication is that at finite temperatures the softening of the phonon energy leads to an avalanche of low-energy phonons and suppression of superfluidity near the spinodal point. Apart from giving the low-density limit of a filled-gap configuration, the spinodal points serves as a valuable consistency check of both the analytical and numerical implementation of the theory of inhomogeneous quantum liquids.

B. Low concentration mixtures

The study of ^{3}He impurities in ^{4}He films *per se* has led to much exciting physics and deeper understanding of the physical mechanisms governing the behavior of confined quantum fluids;[79] we shall see that the behavior is even richer in the situation under investigation here.

The behavior of single ^{3}He impurities in ^{4}He surfaces and within the bulk liquid in both two and three dimensions can be quite accurately described by manifestly microscopic theoretical methods.[55,40,70,80] The first questions to ask are, of course, the solvation energy and spatial distribution of the individual components of the low-concentration mixture.

Before we discuss our results, it is worth recalling the mechanism of ^{3}He mixing in ^{4}He films and in both three- and two-dimensional ^{4}He. In a quantum film, ^{3}He atoms will first populate Andreév states in the surface; the binding energy of these states is about 5 K.[81] That way, a quasi-two-dimensional Fermi liquid of ^{3}He is formed in the surface. Only when the chemical potential of these surface states becomes high enough will ^{3}He atoms penetrate into the bulk liquid. In three-dimensional bulk ^{4}He, the chemical potential of single ^{3}He atoms is -2.2 K,[82] but it increases rapidly with pressure and becomes zero slightly above a density of 0.023 Å^{-3}. The ^{3}He impurity is, on the other hand, unbound in two-dimensional ^{4}He.

In the systems under consideration here, we have in principle no free surface. Nevertheless, in cases with low areal density, we have a rather dilute ^{4}He liquid in the middle of the gap. Hence, at low areal density, one expects that the ^{3}He atoms will populate states close to the center of the gap, but attached to ^{4}He areas that resemble a free surface. The binding energies of such impurity states should be about twice the binding energy of an Andreév state because the ^{3}He impurity ''sees'' two ^{4}He surfaces.

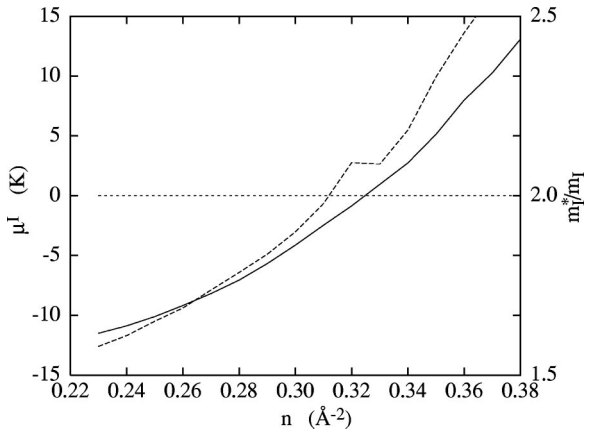

FIG. 10. The figure shows the binding energy (solid line, left scale) and the effective mass (dashed line, right scale) of ^{3}He impurities within ^{4}He filling a 14-Å-wide gap as function of areal density n.

As the ^{4}He areal density is increased, any resemblance of the center area to a free surface disappears, and the system becomes essentially a two-dimensional liquid. The impurity is affected by this in two ways: First, the larger zero-point motion of the ^{3}He atom causes the impurities to stay away from the walls, and second, the chemical potential should become positive.

Both of these effects are seen clearly in the energetics of the impurity and its location within the ^{4}He host liquid. The energetics of ^{3}He atoms in our confined ^{4}He liquids is shown in Fig. 10 and the density profiles in Fig. 11. At low ^{4}He density, the ^{3}He atoms occupy ''Andreév-like'' states in the center of the film. We see indeed that the binding energy at low areal densities is about twice the binding energy of the Andreév state, but it increases rapidly and goes through zero at about the two-dimensional density where the transition of a four-layer to a five-layer system occurs. At the same areal density, the ^{3}He state turns from a rather broad feature to a very narrowly peaked wave function in the center of the films, as seen in Fig. 11: As the density is increased, the ^{3}He atoms are repelled by the high ^{4}He density at the walls, and become strongly localized in the center of the gap, forming an almost perfect two-dimensional Fermi gas.

A close-up of the situation is shown in Fig. 12. There, we

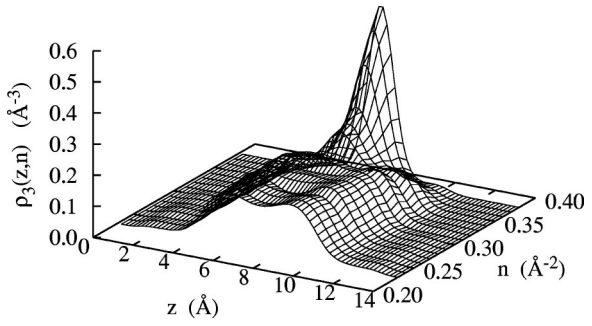

FIG. 11. Locations of ^{3}He impurities within ^{4}He filling a 14-Å-wide gap are shown as functions of areal density n between $n=0.23$ Å^{-2} and $n=0.38$ Å^{-2}.

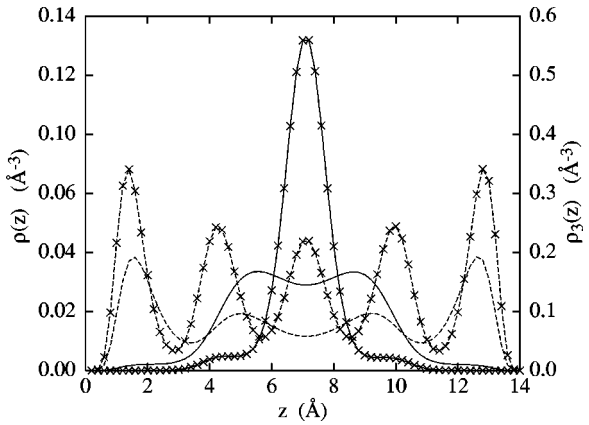

FIG. 12. The figure shows a comparison between the ^{4}He background densities (dashed lines) and the location of the ^{3}He impurities (solid lines) in the 14-Å-wide gap for the two extreme densities $n=0.23$ Å^{-2} (no markers) and $n=0.38$ Å^{-2} (lines marked with crosses).

show a comparison of the density profiles for the ^{4}He liquid and the ^{3}He impurity for a very low and a very high background density. At the low density $n=0.23$ Å^{-2}, the ^{4}He is modly localized at the walls; the local density there reaches almost twice the bulk saturation density, whereas the density in the center is well below the bulk saturation density. The ^{3}He is spread out over the innermost two layers of the ^{4}He film where it is most strongly bound. At the high density, on the other hand, the ^{3}He impurity overlaps practically only with the innermost ^{4}He layer.

We mention in passing that in contrast, the nonlocal density functional theory,[83] which has also been used in the two-walled geometry studied here,[30] predicts mixing near the walls.[84] The reason is that the density functional associates a density-dependent effective mass with the ground state of the ^{3}He particle, whereas a proper microscopic treatment associates an effective mass only with the level density of excitations.[55]

Along with the binding energy, we show in Fig. 10 also the effective mass of the ^{3}He impurity for motion in the x-y

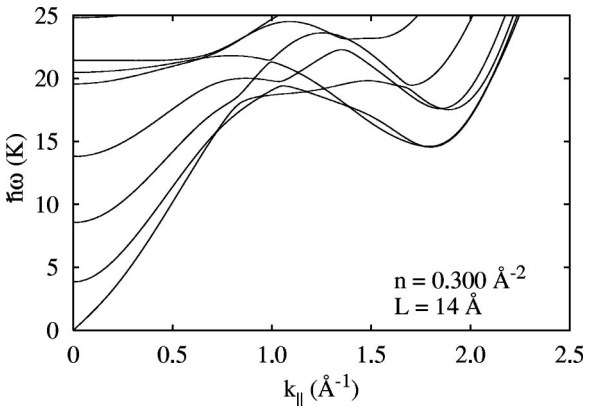

FIG. 13. The excitation spectrum in the Feynman approximation in a 14-Å-wide gap at the areal density $n=0.300$ Å^{-2}. In this approximations modes are not decaying and we plot here only the positions of the δ-function peaks in $S(k_\parallel,\omega)$.

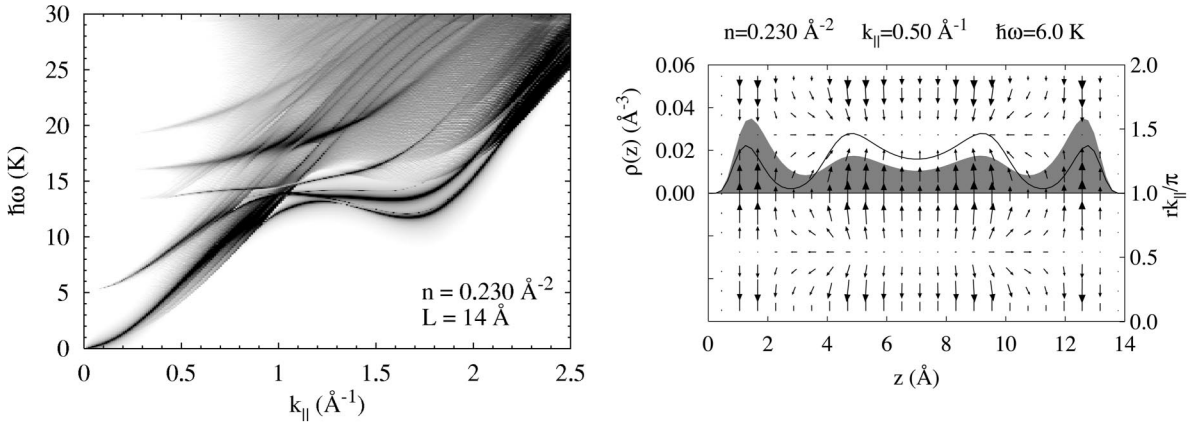

FIG. 14. Left figure: the dynamic structure function $S(k_\parallel;\omega)$ parallel to the symmetry plane for areal density 0.23 Å^{-2}, close to the spinodal instability of the filled-gap configuration. The magnitude of $S(k_\parallel;\omega)$ is indicated by the gray scale. Right figure: the particle current at the same areal density of the phonon at $k=0.5$ Å^{-1}. The gray-shaded area depicts the background density, the solid line the transition density corresponding to the excitation, and the superimposed vector field is the particle current flow.

plane. Expectedly, we see a rapid increase of the effective mass as a function of areal density; a small ''kink'' is seen at the location of the layering transition. Considering the rather drastic change of both the ^{4}He environment and the ^{3}He wave function, this signature of the layering transition is actually surprisingly weak.

The effective mass was calculated by the relatively simple formula (3.24); it should, therefore, be considered as qualitative at high areal densities. More accurate evaluations of the ^{3}He effective mass have been carried out in three[85,70] and two[80] dimensions, but these methods have not yet been implemented for the inhomogeneous geometries considered in this paper.

C. Dynamic properties

Let us now turn to the dynamical properties of the confined liquid helium. Again we use the system with gap width 14 Å as an example and reference system, although several of the systematic trends can be revealed only by looking at some of the quantities as a function of the gap width. After briefly describing the Feynman spectra we reassess the spinodal instability and then move on to discuss the behavior of the roton excitations and the angular dependence of the dynamic structure function.

Figure 13 shows the collective excitation energies in Feynman approximation defined by the generalized eigenvalue problem (3.10) at the coverage $n=0.300$ Å^{-2} for the gap width of 14 Å. These modes propagate at frequencies in close proximity to one another (mode crossings are quite common) and can be categorized as being surface modes (at low areal density), layer phonons, and bulklike modes. Notice the absence of a continuum in the spectrum: In one-sided films the excitations spectrum is continuous provided that

$$\hbar\omega > -\mu + \frac{\hbar^2 k_\parallel^2}{2m}, \tag{5.6}$$

but now atoms cannot be moved to arbitrary distance off the liquid; hence *all modes* are described by discrete quantum numbers perpendicular to the symmetry plane. In particular, the $k_\parallel \to 0$ limit is just a discrete set of states at fixed energies. This could give rise to *dispersionless modes* observable in perpendicular scattering. In Refs. 86 and 87 it was argued that, in the case of one-sided films, one can see a pattern of dispersionless modes within the continuum; this provides an interpretation of such modes seen in neutron scattering experiments off helium adsorbed on graphite powder.[88] Here, the situation is even clearer, the discreteness of the spectrum in the $k_\parallel \to 0$ limit is specific to the geometry and will be there also in spectra calculated with more accurate implementations of CBF theory than the one used here.

We are now ready to go beyond the Feynman approximation and turn to the treatment of excitations within the CBF theory. One of the new physical features coming in at that level of treatment is that excitations can *decay.* The left part of Fig. 14 shows the CBF dynamic structure function $S(k_\parallel,\omega)$ calculated from Eqs. (3.1) and (3.16) with the self-energy (3.15) near the spinodal point at $n=0.23$ Å^{-2}. The sound velocity is about to go to zero as expected. The nature of the phonon mode can be visualized by looking at the

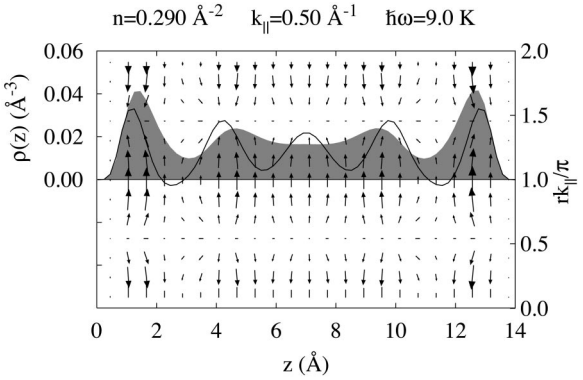

FIG. 15. The transition density and current for the lowest–energy phonon at $n=0.290$ Å^{-2}, right below the confined layering transition. Notice how the density profile has four layers, but the transition density shows that low-momentum excitations already use five layers.

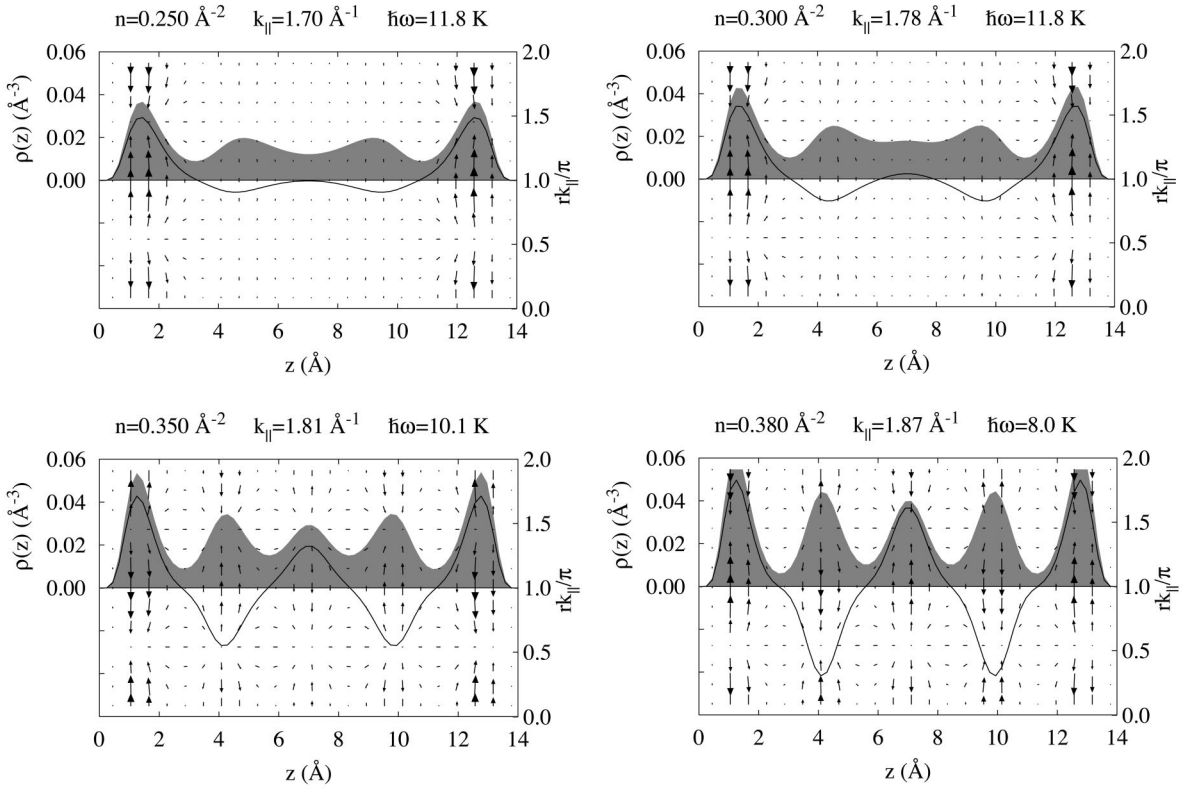

FIG. 16. The transition density and current for the lowest-energy roton at areal densities $n=0.250$, 0.300, 0.350, and 0.380 Å^{-2}.

transition density and current at low-momentum transfer. These are shown in the right part of Fig. 14. The particle current depends on the z coordinate and it is periodic in the direction parallel to the walls; the period is determined by the parallel momentum $k_{\|}$. We plot one period of the current, $0 \leqslant r k_{\|} \leqslant 2\pi$. The transition density is now spread over all layers; hence the spinodal instability corresponds to a vanishing sound velocity of a two–dimensional phonon. The

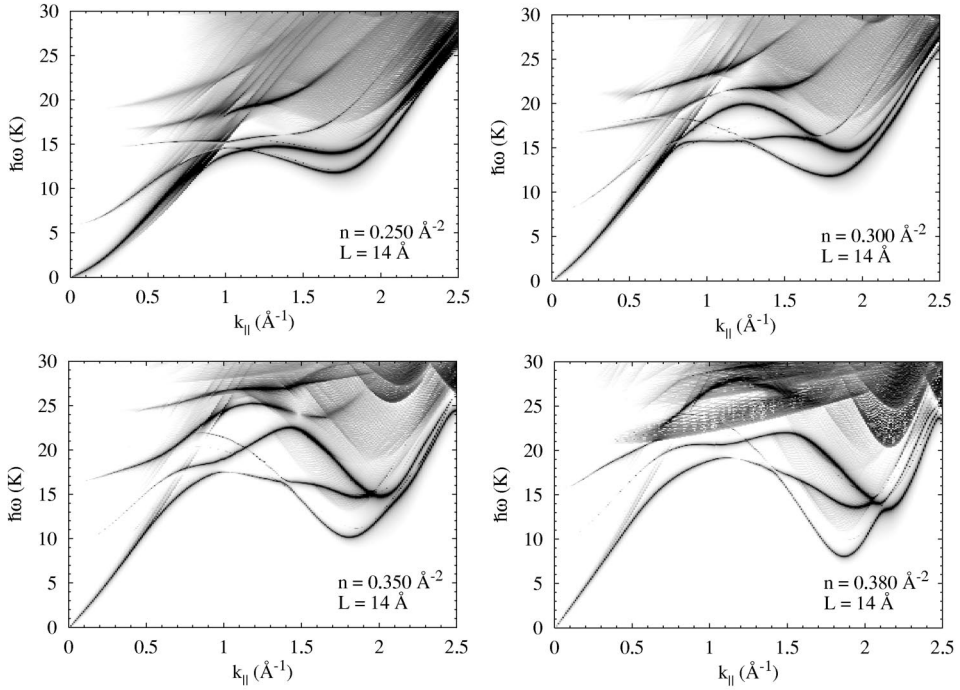

FIG. 17. The dynamic structure functions $S(k_{\|};\omega)$ at the same areal densities as Fig. 16.

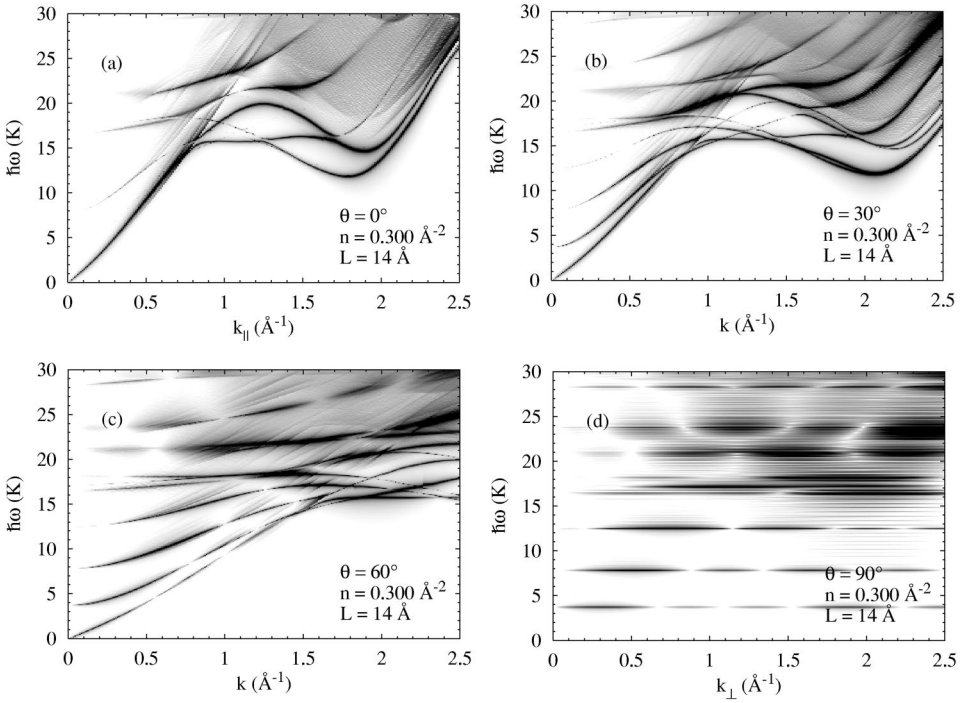

FIG. 18. The dynamic structure function $S(k;\omega)$ at the areal density 0.300 Å^{-2}. The angle between **k** and the symmetry plane is (a) 0°, (b) 30°, (c) 60°, and (d) 90°.

particle currents show that the excitation is basically longitudinal.

Figure 15 shows the transition density and current at the areal density $n=0.290$ Å^{-2}. This is *below* the four- to a five-layer transition, and although there is no sign of a fifth layer in the density profile (depicted by the gray-shaded area in the figure), the transition density already anticipates that a fifth layer is about to emerge.

It is suggestive to look for a signature of confined layering in the excitation spectra. The transition from four to five layers was discussed in Ref. 2. There, we showed that for the gap width of 14 Å the roton energy drops rapidly above the transition. We have now conducted a systematic study of this effect as a function of the gap width. Surprisingly, the roton energy seems to be sensitive to the layering transition from two to three and four to five layers, but not from three to four layers. For more than five layers the effect is smeared out, and a systematic difference between transitions from odd to even and even to odd number of layers cannot be verified. In most cases the roton energy decreases with increasing areal density but in the four-layer configuration the roton energy stays nearly constant.

The transition densities and currents corresponding to the lowest-energy roton are depicted in Fig. 16 (see also Fig. 17). The figure shows that at low areal densities the roton is propagating symmetrically in the two high-density layers close to the walls. At higher areal densities the excitation spreads out and is basically in resonance with the density profile throughout the film; in other words, we can identify it with a longitudinal ''volume'' excitation.

The angle dependence of the dynamic structure function is shown in Fig. 18 for the areal density $n=0.300$ Å^{-2}. Scattering not parallel to the symmetry plane contributes, for example, in experiments done on powder samples with ran-

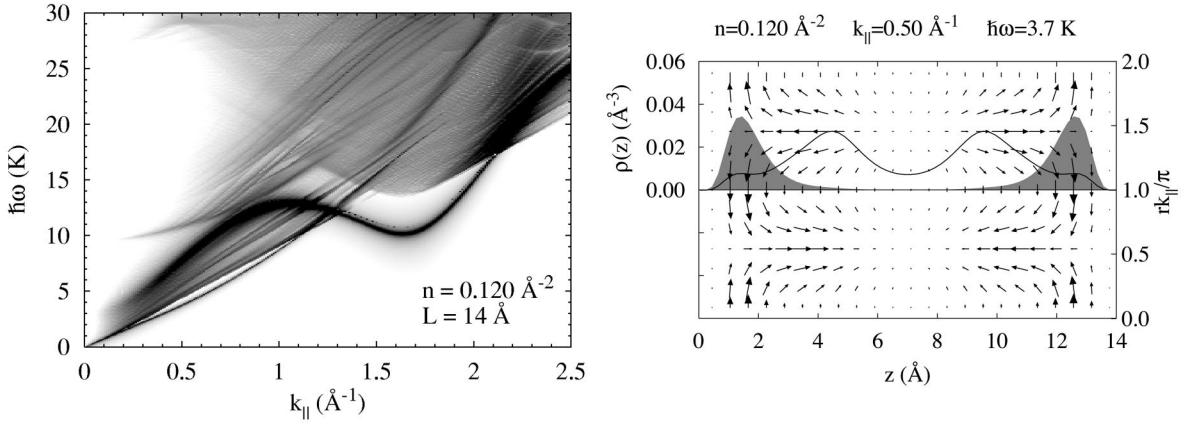

FIG. 19. Left figure shows the dynamic structure function $S(k_{\|};\omega)$ at the areal density 0.120 Å^{-2}. The low-energy excitation is a ripplon. The right figure plots the transition density and current at $k_{\|}=0.5$ Å^{-1}.

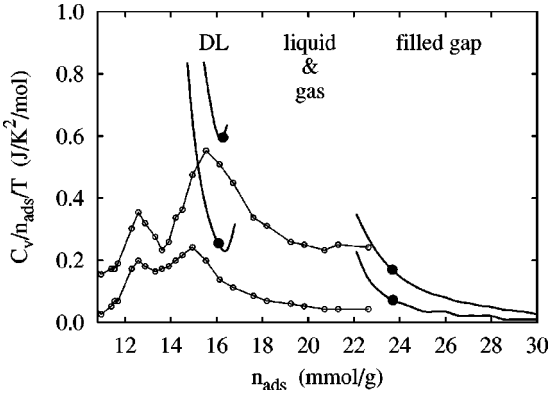

FIG. 20. The specific heat of the two-wall system (thick solid lines) compared with the hectorite experimental data given in Ref. 27 (open circles connected by a thin line) at $T=0.2$ and 0.6 K (upper curves). The specific heat was calculated using Eq. (5.8). Solid black dots indicate phase transitions obtained using the tangent construction shown in Fig. 21.

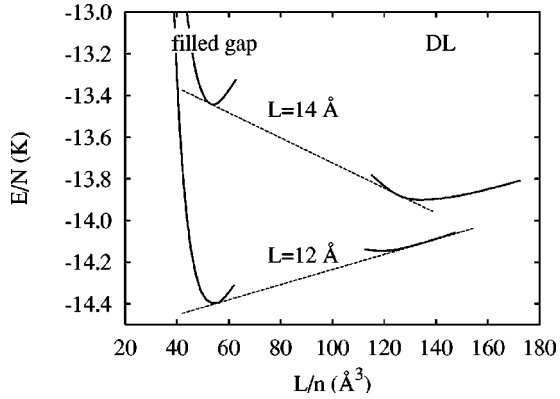

FIG. 21. The figure shows the tangent (Maxwell) construction between a filled-gap and a symmetric double-layer (DL) structure for two gap widths indicated in the picture at $T=0$. For $L=12$ Å the double-layer solution is on the verge of becoming unstable.

domly oriented grains. In this case the observed excitations spectrum is angle averaged, and one may recognize features characteristic to perpendicular scattering: If the momentum transfer is perpendicular to the walls, the spectrum is made of dispersionless stripes. The underlying spectral density consists of maxima which follow the shape of the phonon-roton spectrum of bulk helium. The roton energy in the perpendicular direction is, however, slightly higher than the corresponding energy in the parallel direction. The perpendicular scattering measures the density of states at $k_\parallel \rightarrow 0$, whose maximum is above the energy of the parallel roton. This is already apparent in the Feynman approximation: In the $k_\parallel \rightarrow 0$ limit in the spectrum in Fig. 13 the states are closely packed around 20 K, whereas the roton is at about 15 K. The decay of the modes added by the CBF self-energy renormalizes these values, but the result remains qualitatively unchanged.

As long as the liquid has a free surface it can sustain a ripplon excitation. In the left part of Fig. 19 we plot the dynamic structure function parallel to the walls at $n=0.120$ Å^{-3}, which corresponds to a monolayer on each wall. The ripplon is clearly the lowest mode between $k_\parallel \sim 0.3$ and 1.0 Å^{-1}. The right part of Fig. 18 shows the transition density and current at the ripplon excitation. The transition density shows clearly how the excitation propagates on the surface of the liquid, and the transition current has the circulation pattern specific to ripplons.[34] The transition density shows how the liquid attempts to spread to the space between the existing layers, just like it could foresee the appearance of the fifth layer in a four-layer liquid (see Fig. 15).

D. Thermodynamics

As mentioned in the Introduction, the specific heat data of helium in the hectorite environment reported in Ref. 27 cover two-phase regions where the present theory is not applicable, but does not reach our primary interest, the filled-gap region. The substrate potential in hectorite is unknown and the pillars, which hold the silicate layers apart, may act as additional attractors. Present knowledge of hectorite is clearly inadequate for quantitative theoretical studies, and the two-wall model does not account for the finite porosity and connections between hectorite grains. With these provisions, we carry out a comparison between the specific heat of our model system and the experimental results of helium in hectorite reported in Ref. 27.

The results are plotted in Fig. 20 at temperatures $T=0.2$ and 0.6 K. To facilitate the comparison we have converted the areal density n to the adsorbed amount $n_{\rm ads}$. Using the adsorption area $A=592$ m^2/g of the sample used in Ref. 27, the relation reads

$$n_{\rm ads}=(49.15n+10.8)\ \ \text{mmol/g}. \tag{5.7}$$

Here n is given in units of Å^{-2}. The above formula takes into account that about 10.8 mmol/g is needed to fill the solid layer[27] and that the areal density gives the amount of helium per two walls.

For the theoretical specific heat we used the formula given in Ref. 48,

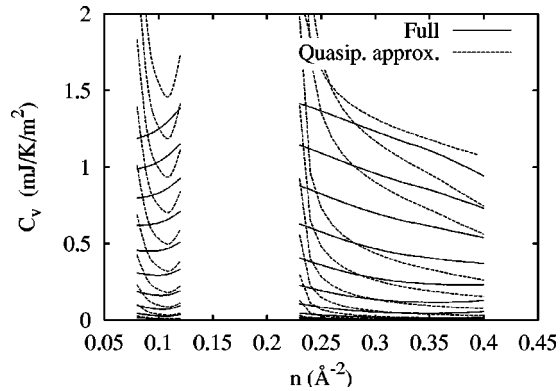

FIG. 22. The theoretical specific heat at $T=0.5,1.0,\ldots,5.0$ K as a function of areal density. The quasiparticle approximation is calculated using the zero-temperature spectrum, whereas the full calculation is the result with spectrum at each temperature.

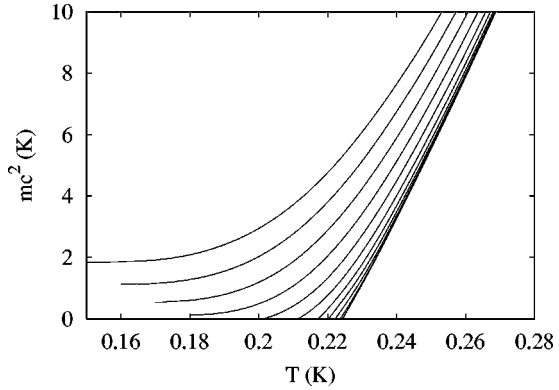

FIG. 23. The figure shows the longitudinal incompressibility for temperatures $T=0,0.5,\ldots,3$ K. The lowest curve corresponds to $T=0$. The width of the gap is 14 Å.

$$C_V=\frac{A}{k_B T^2}\sum_m \int \frac{d^2k_\parallel}{(2\pi)^2}[\hbar\omega_m(k_\parallel)]^2 n_m(k_\parallel)[n_m(k_\parallel)+1], \tag{5.8}$$

where A is the area. We ignore the small contribution coming from the explicit temperature dependence of the excitations energies $\hbar\omega_m(k_\parallel)$ (m is the branch index).

The magnitudes of the specific heat results are roughly the same as the experimental data. The specific heat given by Eq. (5.8) is infinite at spinodal points, but since they lie outside the stable limits determined from a Maxwell construction (solid circles in Fig. 20), the experimentally observable specific heat shows at most smeared maxima.

More can be learned from a comparison of the density scales of helium in the two-wall system and in hectorite. In Fig. 20 we have indicated three regions, as they appear in the *theoretical* results: The symmetric double-layer and filled-gap regions are separated by a mixed-phase region left blank because it is not a translationally invariant configuration. In this coverage area, one has most likely coexistence between a gas and a capillary-condensed liquid. A monolayer, if it were stable, would reside around $n_{\rm ads}\sim 13.3$ mmol/g, near the minimum in the observed specific heat. The sample used in Ref. 27 showed superfluidity above $n_{\rm ads}\sim 14.4$ mmol/g (total of 1.33 layers, one solid layer, and a partially filled liquid layer). This is close to the lowest value where the theoretical model predicts a translationally invariant liquid configuration, a symmetric double layer marked as DL in Fig. 20. The spinodal point of gap filling corresponds to $n_{\rm abs}\approx 22.1$ mmol/g, while the tangent construction shown in Fig. 21 gives as the point of phase transition $n_{\rm abs}\approx 23.7$ mmol/g. These are close to the experimental gap filling in hectorite, which, according to Wada *et al.*, probably corresponds to $n_{\rm ads}\sim 23$ mmol/g. The filling of the gap is accompanied by appearance of a sound mode, so it is expected to show up as a peak in the low-temperature specific heat: A rounded peak was indeed observed at $T=1.7$ K.[27]

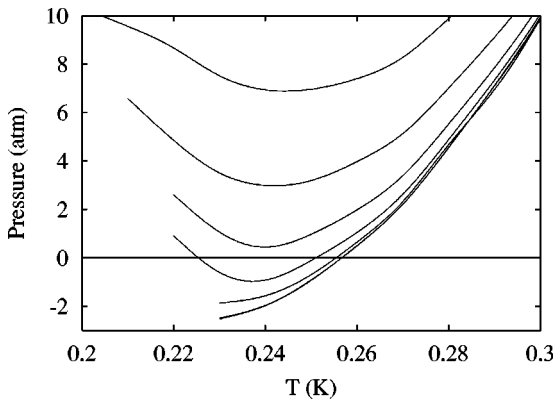

FIG. 24. Same as Fig. 23 but for the pressure.

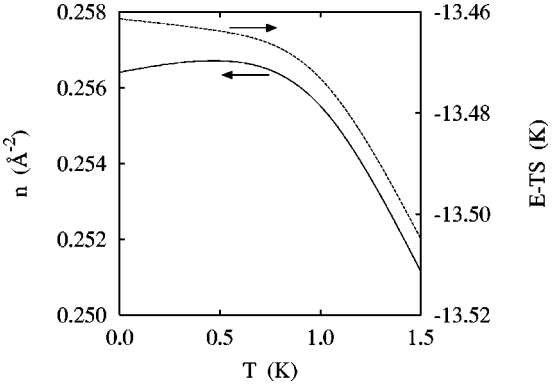

FIG. 25. Temperature dependence of the equilibrium areal density (solid line, left scale) and free energy (dashed line, right scale). No free energy minimum was found above 1.5 K (see also Fig. 26).

The main conclusion that can be drawn based on the theoretical results is that the stability of the low-coverage liquid structures is very sensitive to the gap width. A tangent construction given in Fig. 21 shows that the symmetric double-layer configuration seems to be stable for $L=14$ Å, but is nearly unstable if the gap width is reduced by only 2 Å. Considering that the space available for liquid is not well known, it is not clear whether the double layer is stable or not in the real hectorite environment. Furthermore, stability of the double-layer configuration depends not only on the width of the gap, but also on how attractive the substrate potential is.

For completeness, Fig. 22 plots the theoretical specific heat between 0.5 and 5.0 K. We compare the specific heat

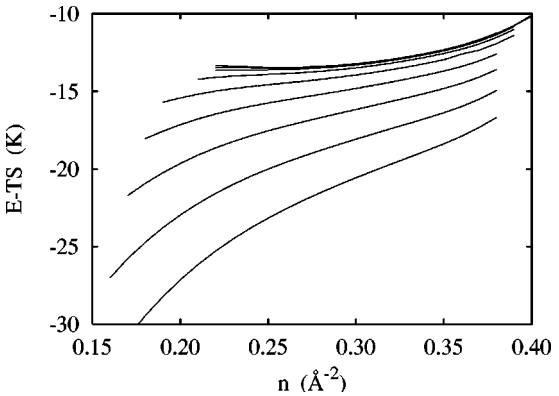

FIG. 26. Free energy as a function of areal density for temperatures $0,0.5,\ldots,5$ K. Lower curves correspond to higher temperature.

calculated from the fully self-consistent calculation, where all distribution functions and effective interactions are temperature dependent, with a ''quasiparticle approximation.'' This approximation is obtained by taking the excitation spectra of a *zero-temperature* calculation in Eq. (5.8) instead of the temperature-dependent spectrum. The steep rises in the quasiparticle approximation for the specific heat are not visible in the full result, because the spinodal instability causing these steep rises moves away from the calculated areal density regime at elevated temperatures.

The temperature dependence of the longitudinal incompressibility of a filled 14-Å gap is shown in Fig. 23, where we plot mc^2 as a function of areal density for temperatures $T=0,0.5,\ldots,3$ K. Figure 24 plots the corresponding pressure for fixed gap width L and particle number N, given by

$$P_L(n,T)=\frac{n^2}{L}\left(\frac{\partial(E-TS)}{\partial n}\right)_{L,N}. \tag{5.9}$$

Figure 25 shows how the equilibrium density and free energy decrease with increasing temperature [the small rise in $n(T)$ at low T can be attributed to numerical inaccuracy]. The net effect is that the sound velocity decreases with temperature, just like in bulk ^{4}He. Above $T=1.5$ K the theoretical free energy has no minimum. As the high-temperature curves in Fig. 26 show, the free energy can be decreased arbitrarily upon reduction of the areal density, which tells us that atoms are evaporating to the surrounding vacuum. This two-phase region cannot be described by the present theory, so results for $T>1.5$ K should be considered as tentative.

VI. CONCLUSIONS

We have applied in this paper a state-of-the-art microscopic many-body theory to calculate the structure, dynamics, and thermodynamics of ^{4}He and ^{3}He-^{4}He mixtures confined between two attractive walls. The systems examined here should, above all, be considered as models for hectorite, but are, in a broader sense, also applicable for the more general problem of helium in other confined geometries like Aerogels, Vycor, or solid matrices. We hope that the effects discussed in our work will stimulate experimental interest in these systems, most prominently on hectorite because of its regular structure.

Our ground-state theory has been tested in various geometries such as the bulk liquids in two and three dimensions, in films, and in droplets of helium. In all cases where exact simulation results or experiments are available, it has been of excellent accuracy. There is no reason to assume that this would not be the case in the systems considered here; we expect therefore that the largest uncertainty of our structural results stems from the external field.

More approximations have been made for the calculation of excited states and thermodynamic properties. In their essence, these approximations amount to the use of the Feynman spectrum in the energy denominators of Eqs. (3.15) and (3.22). In fact, when the Feynman spectrum in these expressions is replaced by a spectrum that resembles essentially the phonon-roton curve, the discrepancy between theory and experiment is reduced to a few percent. A proper refinement of the theory to that level is, of course, much more complicated; we shall postpone such efforts until systematic experiments on the systems examined here are performed.

The most prominent effects that appeared in our studies are the layering transitions. We have studied systematically the observable signatures of such transitions; the most promising is the predicted drop of the energy of the lowest roton. The layering transitions also give rise to oscillations in the pressure exerted on the walls and, as we discussed in Ref. 2, the perpendicular, high-momentum static density-density response function $\mathcal{X}_\perp(k,\omega=0)$ changes discontinuously. Of course, the layering transitions should show up in any quantity which is sensitive to structural changes on the scale of few angstroms. Just what to expect in an experiment on hectorite is very difficult to assess: there are three important length scales stemming from the gap width, the substrate potential, and the short-range He-He repulsion, but only the last one is well known.

A point worth mentioning, but which has not been addressed in this work, is the interaction between ^{3}He impurities. We have shown earlier[80,89] that ^{3}He impurities form, in two dimensions, *dimers* at low ^{3}He concentration. This dimerization has been predicted by Bashkin[90] on very general grounds. The binding energy of ^{3}He dimers in purely two-dimensional ^{4}He is of the order of microkelvins; in other words, the effect would be quite hard to detect experimentally, especially since the systems that come closest to two-dimensional ^{4}He are atomic monolayers on strong substrates. These substrates must be strong enough to prevent the promotion of the ^{3}He impurities to Andreév states. The downside of such strong substrates is the possible corrugation effects, which make the formation and observation of very loosely bound dimers difficult.

We expect that the dimerization effect is more pronounced in the geometry studied here because the dimerization is basically due to the exchange of phonons. At low areal density, these phonons are relatively soft modes which are, therefore, more attractive than two-dimensional phonons. At areal density above the layering transition, the ^{3}He subsystem looks very much like a proper 2D system; we expect the binding energy therefore to be comparable to the one found in Ref. 89. We have refrained from calculating the ^{3}He dimer binding energy in this work since the resulting Schrödinger equation is a truly three-dimensional eigenvalue problem which requires large-scale computational techniques for its solution. This is feasible today; hence there is little justification in approximate treatments. But the effort is beyond the scope of this work, results will be reported elsewhere.

ACKNOWLEDGMENT

This work was supported by the Austrian Science Fund (FWF) under Project No. P12832-TPH.

[1] R. Evans, in *Liquids and Interfaces*, edited by J. Charvolin, J. F. Joanny, and J. Zinn-Justin (Elsevier, Amsterdam, 1990).
[2] V. Apaja and E. Krotscheck, J. Low Temp. Phys. **123**, 241 (2001).
[3] M. P. Lilly, P. T. Finley, and R. B. Hallock, Phys. Rev. Lett. **71**, 4186 (1993).
[4] M. P. Lilly, A. H. Wootters, and R. B. Hallock, Phys. Rev. Lett. **77**, 4222 (1996).
[5] A. H. Wootters and R. B. Hallock, Physica B **284-288**, 141 (2000).
[6] J. de Kinder, G. Goddens, and R. Millet, Z. Phys. B: Condens. Matter **95**, 511 (1994).
[7] O. Plantevin, B. Fåk, H. R. Glyde, J. Bossy, and J. R. Beamish, Phys. Rev. B **57**, 10 775 (1998).
[8] R. M. Dimeo, P. E. Sokol, C. R. Anderson, W. G. Stirling, and M. A. Adams, J. Low Temp. Phys. **113**, 369 (1998).
[9] B. Fåk, O. Plantevin, and H. R. Glyde, Physica B **276-278**, 806 (2000).
[10] P. E. Sokol, M. R. Gibbs, W. G. Stirling, R. T. Azuah, and M. A. Adams, Nature (London) **379**, 616 (1996).
[11] M. R. Gibbs, P. E. S. W. G. Stirling, R. T. Azuah, and M. A. Adams, J. Low Temp. Phys. **107**, 33 (1997).
[12] C. R. Anderson, K. H. Andersen, J. Bossy, W. G. Stirling, R. M. Dimeo, P. E. Sokol, J. C. Cook, and D. W. Brown, Phys. Rev. B **59**, 13 588 (1999).
[13] R. B. Hallock, Phys. Today **51** (6), 30 (1998).
[14] F. Mugele and M. Salmeron, Phys. Rev. Lett. **84**, 5796 (2000).
[15] B. N. J. Persson and E. Tosatti, Phys. Rev. B **50**, 5590 (1994).
[16] B. N. J. Persson, Chem. Phys. Lett. **324**, 231 (2000).
[17] B. N. J. Persson and P. Ballone, J. Chem. Phys. **112**, 9524 (2000).
[18] J. Gao, W. D. Luedtke, and U. Landman, Phys. Rev. Lett. **79**, 705 (1997).
[19] J. Crassous, E. Charlaix, and J. L. Loubet, Europhys. Lett. **28**, 37 (1994).
[20] J. Crassous, E. Charlaix, and J. L. Loubet, Phys. Rev. Lett. **78**, 2425 (1997).
[21] J. A. Lipa, D. R. Swanson, J. A. Nissen, Z. K. Geng, P. R. Williamson, D. A. Stricker, T. C. P. Chui, U. E. Israelsson, and M. Larson, Phys. Rev. Lett. **84**, 4894 (2000).
[22] I. Rhee, F. M. Gasparini, and D. J. Bishop, Phys. Rev. Lett. **63**, 410 (1989).
[23] S. Mehta, M. O. Kimball, and F. M. Gasparini, J. Low Temp. Phys. **113**, 435 (1998).
[24] S. Mehta, M. O. Kimball, and F. M. Gasparini, J. Low Temp. Phys. **114**, 467 (1999).
[25] M. O. Kimball and F. M. Gasparini, Physica B **284-288**, 47 (2000).
[26] M. Hieda, M. Suzuki, K. Torii, H. Yano, and N. Wada, J. Low Temp. Phys. **113**, 363 (1998).
[27] N. Wada, A. Inoue, H. Yano, and K. Torii, Phys. Rev. B **52**, 1167 (1996).
[28] M. Hieda, M. Suzuki, K. Torii, H. Yano, and N. Wada, Physica B **263-264**, 370 (1999).
[29] M. Hieda, M. Suzuki, H. Yano, N. Wada, and K. Torii, Physica B **284-288**, 125 (2000).
[30] E. Cheng, M. R. Swift, and M. W. Cole, J. Chem. Phys. **99**, 4064 (1993).
[31] M. M. Calbi, F. Toigo, S. M. Gatica, and M. W. Cole, Phys. Rev. B **60**, 14 935 (1999).
[32] B. E. Clements, J. L. Epstein, E. Krotscheck, and M. Saarela, Phys. Rev. B **48**, 7450 (1993).
[33] E. Krotscheck, *Microscopic Quantum Many-Body Theories and their Applications* (Springer, Heidelberg, 1988), pp. 187–250.
[34] B. E. Clements, H. Forbert, E. Krotscheck, H. J. Lauter, M. Saarela, and C. J. Tymczak, Phys. Rev. B **50**, 6958 (1994).
[35] B. E. Clements, E. Krotscheck, and C. J. Tymczak, Phys. Rev. B **53**, 12 253 (1996).
[36] C. E. Campbell and E. Feenberg, Phys. Rev. **188**, 396 (1969).
[37] C. E. Campbell, Phys. Lett. **44A**, 471 (1973).
[38] C. C. Chang and C. E. Campbell, Phys. Rev. B **15**, 4238 (1977).
[39] E. Krotscheck, Phys. Rev. B **33**, 3158 (1986).
[40] E. Krotscheck and M. Saarela, Phys. Rep. **232**, 1 (1993).
[41] E. Krotscheck, Phys. Rev. B **31**, 4258 (1985).
[42] E. Feenberg, *Theory of Quantum Fluids* (Academic, New York, 1969).
[43] B. E. Clements, J. L. Epstein, E. Krotscheck, and M. Saarela, Phys. Rev. B **48**, 7450 (1993).
[44] A. D. Jackson, A. Lande, and R. A. Smith, Phys. Rep. **86**, 55 (1982).
[45] A. D. Jackson, A. Lande, and R. A. Smith, Phys. Rev. Lett. **54**, 1469 (1985).
[46] E. Krotscheck, R. A. Smith, and A. D. Jackson, Phys. Rev. A **33**, 3535 (1986).
[47] E. Krotscheck, Phys. Rev. B **31**, 4258 (1985).
[48] C. E. Campbell, B. E. Clements, E. Krotscheck, and M. Saarela, Phys. Rev. B **55**, 3769 (1997).
[49] K. R. Atkins, Physica (Amsterdam) **23**, 1143 (1957).
[50] K. R. Atkins, Phys. Rev. **113**, 962 (1959).
[51] D. Goodstein, Phys. Rev. **183**, 327 (1969).
[52] J. L. Epstein and E. Krotscheck, Phys. Rev. B **37**, 1666 (1988).
[53] E. Krotscheck, Phys. Rev. A **15**, 397 (1977).
[54] E. Krotscheck and C. J. Tymczak, Phys. Rev. B **45**, 217 (1992).
[55] B. E. Clements, E. Krotscheck, and M. Saarela, Phys. Rev. B **55**, 5959 (1997).
[56] E. Krotscheck, M. Saarela, and J. L. Epstein, Phys. Rev. B **38**, 111 (1988).
[57] H. W. Jackson, Phys. Rev. A **4**, 2386 (1971).
[58] C. E. Campbell, in *Progress in Liquid Physics*, edited by C. A. Croxton (Wiley, London, 1977), Chap. 6, pp. 213–308.
[59] P. Kramer and M. Saraceno, *Geometry of the Time-Dependent Variational Principle in Quantum Mechanics*, Vol. 140 of *Lecture Notes in Physics* (Springer, Berlin, 1981).
[60] A. K. Kerman and S. E. Koonin, Ann. Phys. (N.Y.) **100**, 332 (1976).
[61] M. Saarela, Phys. Rev. B **33**, 4596 (1986).
[62] M. Saarela and J. Suominen, in *Condensed Matter Theories*, edited by J. S. Arponen, R. F. Bishop, and M. Manninen (Plenum, New York, 1988), Vol. 3, pp. 157–165.
[63] J. Suominen and M. Saarela, in *Condensed Matter Theories*, edited by J. Keller (Plenum, New York, 1989), Vol. 4, p. 377.
[64] R. P. Feynman, Phys. Rev. **94**, 262 (1954).
[65] R. P. Feynman and M. Cohen, Phys. Rev. **102**, 1189 (1956).
[66] C. C. Chang and C. E. Campbell, Phys. Rev. B **13**, 3779 (1976).
[67] H. W. Jackson and E. Feenberg, Rev. Mod. Phys. **34**, 686 (1962).
[68] H. W. Jackson, Phys. Rev. A **8**, 1529 (1973).
[69] V. Apaja and M. Saarela, Phys. Rev. B **57**, 5358 (1998).
[70] E. Krotscheck, J. Paaso, M. Saarela, K. Schörkhuber, and R. Zillich, Phys. Rev. B **58**, 12 282 (1998).

[71] C. E. Campbell, K. E. Kürten, M. L. Ristig, and G. Senger, Phys. Rev. B **30**, 3728 (1984).
[72] G. Senger, M. L. Ristig, K. E. Kürten, and C. E. Campbell, Phys. Rev. B **33**, 7562 (1986).
[73] B. E. Clements and C. E. Campbell, Phys. Rev. B **46**, 10 957 (1992).
[74] B. E. Clements, E. Krotscheck, J. A. Smith, and C. E. Campbell, Phys. Rev. B **47**, 5239 (1993).
[75] G. Vidali, G. Ihm, H.-Y. Kim, and M. W. Cole, Surf. Sci. Rep. **12**, 133 (1991).
[76] C. E. Campbell, R. Folk, and E. Krotscheck, J. Low Temp. Phys. **105**, 13 (1996).
[77] S. Giorgini, J. Boronat, and J. Casulleras, Phys. Rev. B **54**, 6099 (1996).
[78] M. Heni and H. Lowen, Phys. Rev. Lett. **85**, 3668 (2000).
[79] R. B. Hallock, *The Properties of Multilayer ^{3}He-^{4}He Mixture Films*, Progress in Low Temp. Phys. (North-Holland, Amsterdam, 1995), Vol. XIV, Chap. 5, pp. 321–443.
[80] E. Krotscheck, J. Paaso, M. Saarela, and K. Schörkhuber, Phys. Rev. B **64**, 054504 (2001).
[81] D. T. Sprague, N. Alikacem, P. A. Sheldon, and R. B. Hallock, Phys. Rev. Lett. **72**, 384 (1994).
[82] R. de Bruyn Ouboter and C. N. Yang, Physica B **144**, 127 (1986).
[83] N. Pavloff and J. Treiner, J. Low Temp. Phys. **83**, 331 (1991).
[84] L. Pricaupenko and J. Treiner, Phys. Rev. Lett. **74**, 430 (1995).
[85] E. Krotscheck, M. Saarela, K. Schörkhuber, and R. Zillich, Phys. Rev. Lett. **80**, 4709 (1998).
[86] V. Apaja, H. Godfrin, E. Krotscheck, and H. Lauter, J. Low Temp. Phys. (to be published).
[87] E. Krotscheck, M. D. Miller, and R. Zillich, Physica B **280**, 59 (2000).
[88] H. J. Lauter, H. Godfrin, and H. Wiechert, in *Proceedings of the Second International Conference on Phonon Physics*, edited by J. Kollàr, N. Kroo, M. Meynhard, and T. Siklos (World Scientific, Singapore, 1985), p. 842.
[89] E. Krotscheck, J. Paaso, M. Saarela, and K. Schörkhuber, Phys. Rev. Lett. **85**, 2344 (2000).
[90] E. P. Bashkin, Sov. Phys. JETP **51**, 181 (1980).